

Twenty years of experimental and direct numerical simulation access to the velocity gradient tensor: What have we learned about turbulence?

Cite as: Phys. Fluids **21**, 021301 (2009); <https://doi.org/10.1063/1.3046290>

Submitted: 01 July 2008 . Accepted: 01 October 2008 . Published Online: 10 February 2009

James M. Wallace



View Online



Export Citation

ARTICLES YOU MAY BE INTERESTED IN

[Wall-bounded turbulent flows at high Reynolds numbers: Recent advances and key issues](#)

Physics of Fluids **22**, 065103 (2010); <https://doi.org/10.1063/1.3453711>

[Direct numerical simulation of turbulent channel flow up to \$Re_\tau=590\$](#)

Physics of Fluids **11**, 943 (1999); <https://doi.org/10.1063/1.869966>

[Hairpin vortex organization in wall turbulence](#)

Physics of Fluids **19**, 041301 (2007); <https://doi.org/10.1063/1.2717527>



Highlights of the best new research
in the physical sciences

LEARN MORE!





Twenty years of experimental and direct numerical simulation access to the velocity gradient tensor: What have we learned about turbulence?^{a)}

James M. Wallace

Department of Mechanical Engineering, University of Maryland, College Park, Maryland 20742, USA

(Received 1 July 2008; accepted 1 October 2008; published online 10 February 2009)

Twenty years ago there was no experimental access to the velocity gradient tensor for turbulent flows. Without such access, knowledge of fundamental and defining properties of turbulence, such as vorticity dissipation, and strain rates and helicity, could not be studied in the laboratory. Although a few direct simulations at very low Reynolds numbers had been performed, most of these did not focus on properties of the small scales of turbulence defined by the velocity gradient tensor. In 1987 the results of the development and first successful use of a multisensor hot-wire probe for simultaneous measurements of all the components of the velocity gradient tensor in a turbulent boundary layer were published by Balint *et al.* [*Advances in Turbulence: Proceedings of the First European Turbulence Conference* (Springer-Verlag, New York, 1987), p. 456]. That same year measurements of all but one of the terms in the velocity gradient tensor were carried out, although not simultaneously, in the self-preserving region of a turbulent circular cylinder wake by Browne *et al.* [*J. Fluid Mech.* **179**, 307 (1987)], and the first direct numerical simulation (DNS) of a turbulent channel flow was successfully carried out and reported by Kim *et al.* [*J. Fluid Mech.* **177**, 133 (1987)], including statistics of the vorticity field. Also in that year a DNS of homogeneous shear flow by Rogers and Moin [*J. Fluid Mech.* **176**, 33 (1987)] was published in which the authors examined the structure of the vorticity field. Additionally, Ashurst *et al.* [*Phys. Fluids* **30**, 2343 (1987)] examined the alignment of the vorticity and strainrate fields using this homogeneous shear flow data as well as the DNS of isotropic turbulence of Kerr [*J. Fluid Mech.* **153**, 31 (1985)] who had initiated such studies. Furthermore, Metcalfe *et al.* [*J. Fluid Mech.* **184**, 207 (1987)] published results from their direct simulation of a temporally developing planar mixing layer in which they examined coherent vortical states resulting from secondary instabilities. Since then several experimentalists have used multisensor hot-wire probes of increasing complexity in turbulent boundary layers, wakes, jets, mixing layers, and grid flows. Numerous computationalists have employed DNS in a wide variety of turbulent flows at ever increasing Reynolds numbers. Particle image velocimetry and other optical methods have been rapidly developed and advanced during these two decades which have provided other means of access to these fundamental properties of turbulence. This paper reviews highlights of these remarkable developments and points out some of the most important things we have learned about turbulence as a result. © 2009 American Institute of Physics. [DOI: 10.1063/1.3046290]

I. INTRODUCTION

Beginning a little over 40 years ago, experimentalists began discovering that ordered or “coherent” structures play an important, perhaps even a dominant role in the processes of heat, mass, and momentum transport in turbulent flows where they had previously been undetected. Visualization investigations, such as those of Kline *et al.*¹ and Corino and Brodkey² in bounded turbulent flows and Brown and Roshko³ in a turbulent mixing layer demonstrated conclusively the ubiquitous presence of these structures and provided some indication of their dynamical significance. For the mixing layer, the most obviously observable coherent structures were large scale “roller” vortices oriented principally in the spanwise direction. These vortices are generated

by Kelvin–Helmholtz instabilities as are similar spanwise or azimuthal vortices in turbulent wakes and jets. Later, for all these free shear flows, smaller scale “rib” vortices oriented principally in the streamwise plane were detected (e.g., Konrad⁴), as seen in Fig. 1.

It was suspected that the low-speed streak, ejection, and sweep structures visually observed in bounded flows were caused by vortices oriented principally in the streamwise plane, and visual evidence for this supposition later came from Head and Bandyopadhyay.⁵ A sketch of such vortices in wall flows is shown in Fig. 2 from Wallace;⁶ it was based on what could be inferred about the structure of these flows 25 years ago from scant experimental evidence.

However, conspicuously missing during this period were tools to measure vorticity in turbulent flows. In an article about new trends in experimental turbulence research, Laufer⁷ lamented that although “...vorticity measurements suggest themselves as the most promising method for a

^{a)}This paper is based on an invited lecture given by the author at the 60th Annual Meeting of the American Physical Society’s Division of Fluid Dynamics, which was held 18–20 November 2007 in Salt Lake City, Utah.



FIG. 1. (Color online) Rib vortices (above) and roller vortices (below) visualized in a two-stream turbulent mixing layer. From Konrad (Ref. 4 by permission).

quantitative study of ordered motion, unfortunately direct measurement of vorticity has not yet been successfully accomplished with sufficient accuracy.”

Up until as recently as 20 years ago, because there was no capability of measuring the velocity gradient tensor, $A_{ij} \equiv \partial U_i / \partial x_j \equiv S_{ij} + R_{ij}$, where $S_{ij} = \frac{1}{2}(\partial U_i / \partial x_j + \partial U_j / \partial x_i)$ is the strain rate and $R_{ij} = \frac{1}{2}(\partial U_i / \partial x_j - \partial U_j / \partial x_i)$ is the rotation rate, information about the vorticity vector was experimentally inaccessible, as was information about other fundamental properties of turbulence such as the turbulent kinetic energy dissipation rate. A few direct simulations at very low Reynolds number had been performed (e.g., Refs. 8 and 9) but, with the exception of the isotropic simulation of Kerr,¹⁰ most of these did not focus on properties of the small scales of turbulence defined by the velocity gradient tensor.

In 1987 this deficit in knowledge changed significantly. In that year the first measurements of the full velocity gradient tensor, using a miniature nine-sensor hot-wire probe, were presented at the First European Turbulence Conference and were published by Balint *et al.*¹¹ (see also Ref. 12). These measurements provided statistical information about

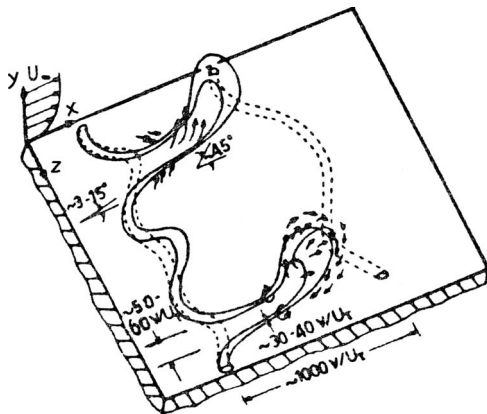


FIG. 2. Conceptual sketch of vortices in wall bounded flows. From Wallace (Ref. 6).

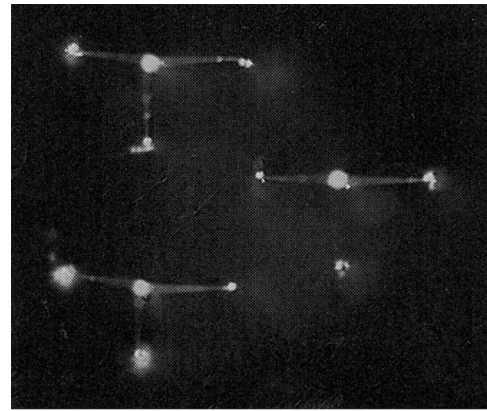


FIG. 3. Photographs of nine-sensor hot-wire probe. From Vukoslavčević *et al.* (Ref. 18). Copyright © 1991 by Cambridge University Press. Reprinted with the permission of Cambridge University Press.

the vorticity field and direct measurements of the full dissipation rate of a turbulent boundary layer. That same year Browne *et al.*¹³ made measurement, although not simultaneously, of all but one of the terms in the velocity gradient tensor in the self-preserving region of a turbulent circular cylinder wake in order to study the dissipation rate. Also that year the first direct numerical simulation (DNS) investiga-

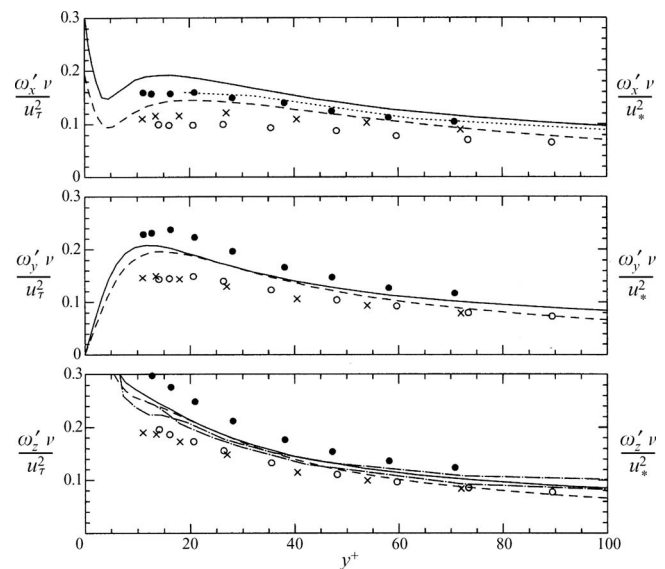


FIG. 4. Experimental and DNS vorticity component rms distributions in bounded flows: \circ (Ref. 28) and \bullet (Ref. 28) with corrected u_τ , \times (Ref. 29), — (Ref. 27), --- (Ref. 14), \cdots (Ref. 30), and - · - (Ref. 31). From Ong and Wallace (Ref. 28). Copyright © 1998 by Cambridge University Press. Reprinted with the permission of Cambridge University Press.

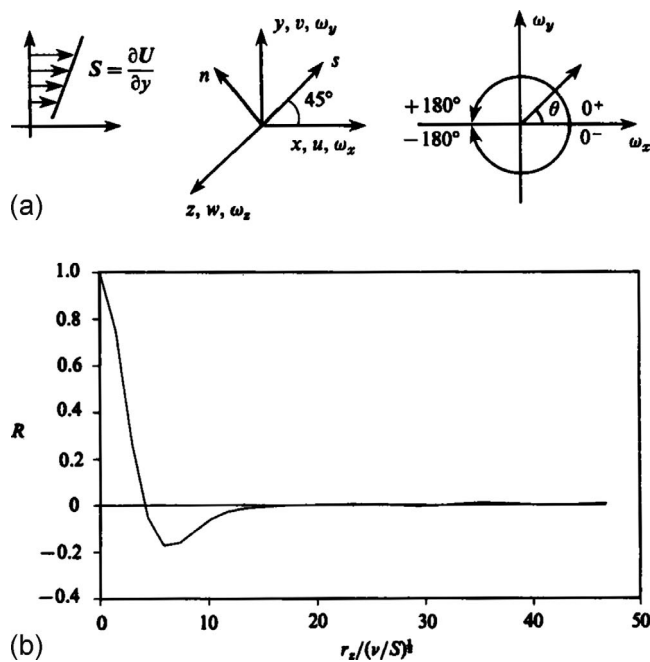


FIG. 5. Coordinate system rotated about the spanwise direction with s -axis oriented in direction of the principal rate of mean strain (above). Spatial correlation R_{ω_s} of vorticity component in the direction of the principal rate of strain in homogeneous shear flow vs $r_z/(v/S)^{1/2}$ (below). From Rogers and Moin (Ref. 16). Copyright © 1987 by Cambridge University Press. Reprinted with the permission of Cambridge University Press.

tions of a turbulent channel flow by Kim *et al.*¹⁴ and of a temporally developing mixing layer by Metcalfe *et al.*¹⁵ were published which made possible the detailed investigation of small scales in these important shear flows. Furthermore, Rogers and Moin¹⁶ published the results from a DNS of homogeneous shear flow in which they examined the structure of the vorticity field, and Ashurst *et al.*¹⁷ studied the alignment properties of small scales using the DNS databases of Rogers and Moin¹⁶ and Kerr.¹⁰ Since then several experimentalists have used multisensor hot-wire probes of increasing complexity in turbulent boundary layers, wakes, jets, mixing layers, and grid flows. Numerous computationalists have employed DNS in a wide variety of turbulent flows at

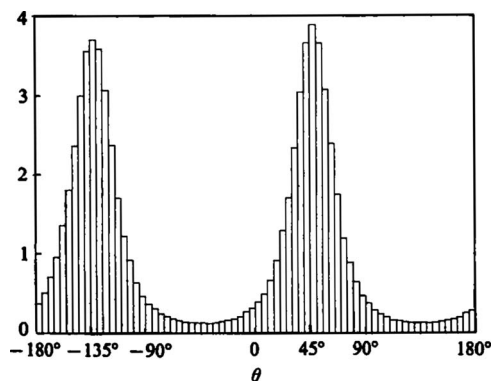


FIG. 6. Histogram of inclination angle of projection of vorticity vectors in the streamwise plane of homogeneous shear flow. Data weighted with the magnitude of the projected vorticity vector. Angle θ defined in Fig. 5. From Rogers and Moin (Ref. 16). Copyright © 1987 by Cambridge University Press. Reprinted with the permission of Cambridge University Press.

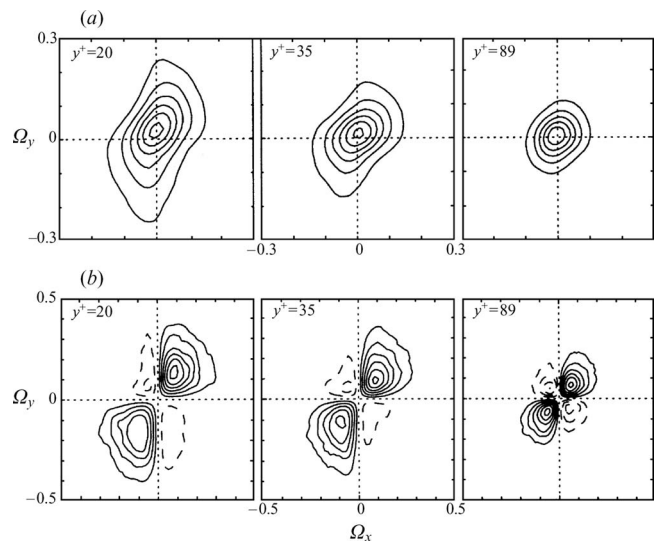


FIG. 7. (a) Streamwise-wall normal vorticity component JPDFs and (b) covariance integrands in the buffer and log layers of a turbulent boundary layer. From Ong and Wallace (Ref. 28). Copyright © 1998 by Cambridge University Press. Reprinted with the permission of Cambridge University Press.

ever increasing Reynolds numbers. Particle image velocimetry (PIV) and other flow imaging methods have been developed and advanced during these two decades. These methods have provided other means of access to these fundamental properties of turbulence. This paper will review and discuss some of the most important things we have learned about turbulence from these remarkable developments in experimental and computational turbulence research capabilities. Sections II and III cover single and joint velocity gradient based properties of turbulence, and Sec. IV discusses the structure of various turbulent flows as revealed by and in relation to these properties.

II. SINGLE VELOCITY GRADIENT BASED TURBULENCE PROPERTIES

A. Vorticity vector

The vorticity vector, a defining property of turbulence, is given by

$$\Omega_i = \epsilon_{ijk} \partial U_k / \partial x_j, \quad (1)$$

where ϵ_{ijk} is the alternating tensor and U_k is the velocity vector with components $U_i = U, V, W$ in the $x_j = x, y, z$ directions. The statistical properties of all three of its components were first measured by Balint *et al.*¹¹ in a turbulent boundary layer with $Re_\theta = 2080$ using the miniature nine-sensor hot-wire probe shown in the photographs in Fig. 3. The six velocity gradients in the cross-stream (y - z) plane that passes through the centers of the sensors are directly determined with this probe. This is done by expanding in Taylor's series to first order the velocity vectors sensed at each sensor center about the geometric center of the probe in this plane. This results in nine nonlinear algebra equations that describe the cooling of each sensor by the flow. These equations are solved iteratively for the six cross-stream plane velocity gradients and the three velocity components that are the un-

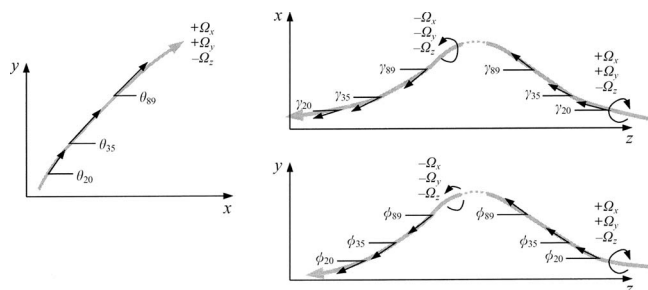


FIG. 8. Projections on the orthogonal coordinate planes of vorticity filament segments making the largest contributions to the vorticity covariances $\overline{\Omega_x \Omega_y}$, $\overline{\Omega_x \Omega_z}$ and $\overline{\Omega_y \Omega_z}$ at $y^+ = 20, 35$ and 89 . From Ong and Wallace (Ref. 28). Copyright © 1998 by Cambridge University Press. Reprinted with the permission of Cambridge University Press.

knowns in the nine equations. The remaining three (streamwise) velocity gradients can be estimated using Taylor's frozen turbulence hypothesis¹⁹ which has been shown to be a fairly good approximation in experiments with enough temporal resolution and in regions of the flow in which the turbulence intensity is not too high. The validity of Taylor's hypothesis for wall bounded flows was examined in Piomelli *et al.*²⁰ Honkan and Andreopoulos²¹ also have developed and used a nine-sensor hot-wire probe to measure vorticity vector properties in a turbulent boundary layer. Details about the fabrication, operation, and spatial resolution of these and the other multisensor probes referred to below can be found in Vukoslavčević and Wallace.²² Several investigations have used 12-sensor probes^{23,24} which provide some redundancy and improved accuracy over the nine-sensor probe. Recently a multisensor probe with twenty sensors has been used in the atmospheric surface layer by Kholmyansky *et al.*²⁵ and later improved to not require Taylor's hypothesis.²⁶

In their ground-breaking DNS of a turbulent channel flow at $Re_\tau = 180$, where τ is the wall shear stress, Kim *et al.*¹⁴ also reported many of these statistical properties of the vorticity vector, as did Spalart²⁷ a year later with DNS of turbulent boundary layers at three Reynolds numbers up to $Re_\theta = 1410$, where θ is the momentum thickness. The channel flow simulation employed a $192 \times 129 \times 160$ node grid and a

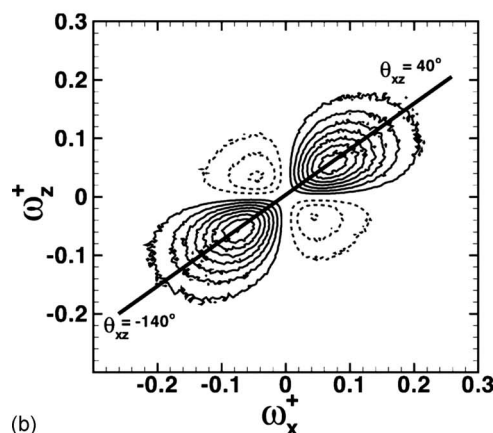
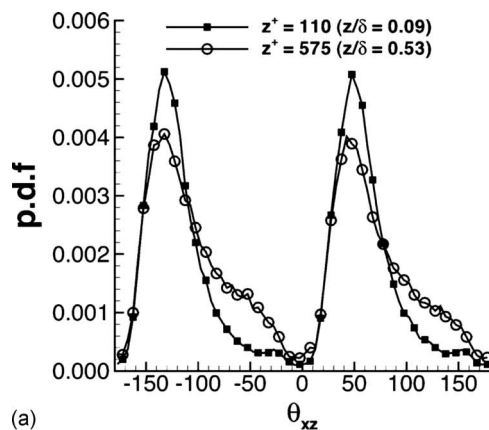


FIG. 10. PDFs of the inclination angle of projection of vorticity vectors on streamwise planes of a turbulent boundary layer (above) (note that z^+ and ω_z^+ in this figure are y^+ and ω_y^+ elsewhere in the present paper). Covariance integrands of ω_x^+ and ω_z^+ at $y^+ = 110$ (below). Reprinted from Ganapathisubramani *et al.* (Ref. 32). Copyright © 2006 by the American Institute of Physics.

spectral numerical method: Fourier series in the streamwise and spanwise directions and a Chebychev polynomial expansion in the wall normal direction. The boundary layer simulation used a $432 \times 80 \times 320$ node grid and also a spectral numerical method: Fourier series in the x - z planes and Jacobi

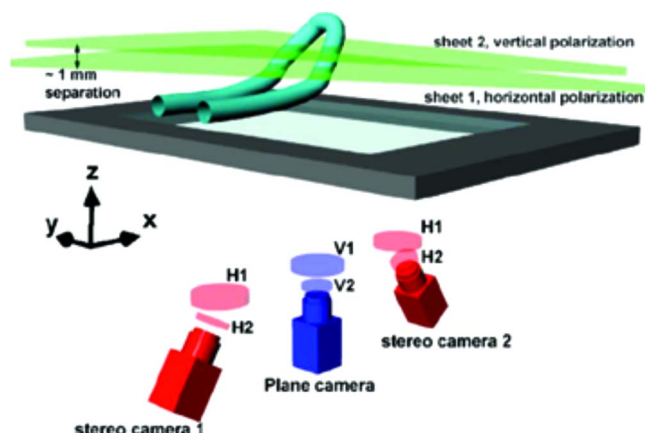


FIG. 9. (Color online) Dual plane PIV turbulent boundary layer experimental arrangement. Reprinted from Ganapathisubramani *et al.* (Ref. 32). Copyright © 2006 by the American Institute of Physics.



FIG. 11. (Color online) Photograph of the 12-sensor hot-wire probe of Vukoslavčević and Wallace (Ref. 24). Each sensor is 0.5 mm long and is inclined at $\approx 45^\circ$ to the flow.

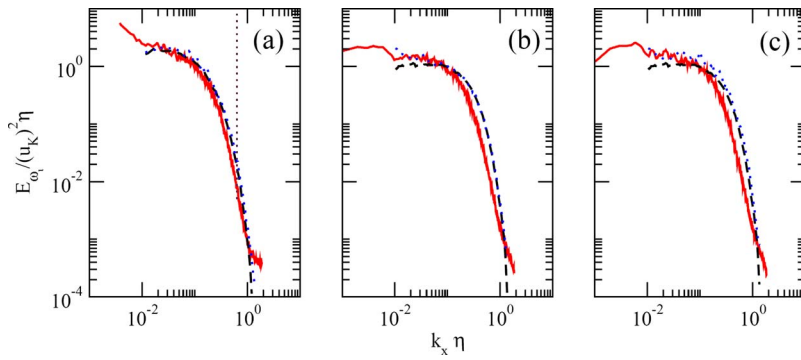


FIG. 12. (Color online) One-dimensional vorticity spectra: (a) streamwise component, (b) wall normal component, (c) spanwise component. (—) Wallace and Ong (Ref. 34) measured with 12-sensor probe in a turbulent boundary layer; (···) channel flow DNS of Kim and Antonia (Ref. 33) and their (---) isotropic calculations. Vertical dotted line indicates scale of the probe. Reprinted from Wallace and Ong (Ref. 34). Copyright © 2008 by the American Institute of Physics.

polynomials in the wall normal direction. In Fig. 4 the root-mean-square vorticity component distributions obtained from these and some other experimental and simulation investigations are compared. Most of the experimental data fall below the two DNS profiles (dashed and solid lines) except for the data (solid circles) of Ong and Wallace²⁸ after the normalizing velocity scale u_τ has been corrected. This correction, the rationale for which was discussed by Ong and Wallace,²⁸ is appropriate because using the Clauser method to determine u_τ , as was done for all the experimental data shown here, results in significantly overestimated values. Furthermore, because u_τ^2 is used to normalize the vorticity component rms values, this error in the normalizing scale is greatly amplified.

Rogers and Moin¹⁶ in a DNS investigation of homogeneous turbulent shear flow with a $128 \times 128 \times 128$ node grid and a turbulence Reynolds number of $Re_\lambda = 72.6$, where λ is the turbulent microscale, calculated two-point vorticity component spatial correlation functions in an orthogonal coordinate system rotated around the spanwise direction. The s -axis in this rotated coordinate system is oriented in the direction of the principal rate of mean strain, and the n -axis is a perpendicular to this direction, as seen in Fig. 5. The $R_{\omega_s \omega_s}$ correlation distribution as a function of the normalized spanwise direction, $r_z/(\nu/S)^{1/2}$, where S is the mean shear rate, is also shown in the figure. The prominent negative dip in the correlation function is clear evidence that, on average, this component of vorticity changes sign, implying some sort of counter-rotational activity in the n - z plane of the vorticity field.

Rogers and Moin¹⁶ also calculated histograms of the inclination angle of the projection of the vorticity vectors on the x - y streamwise plane, with the data weighted with the magnitude of the projected vorticity vector $(\Omega_x^2 + \Omega_y^2)^{1/2}$. The histogram, shown in Fig. 6, exhibits sharp peaks at $\theta = 45^\circ$ and 135° , i.e., the principal direction of mean strain s , implying that the vortex lines, projected on this plane and associated with strong vorticity magnitude, are mainly oriented in this direction.

Another way to look at the orientation of the vortex lines in a turbulent flow is to plot the joint probability density distributions (JPDFs) of the vorticity components. Ong and Wallace²⁸ did this using data from a nine-sensor probe taken in a turbulent boundary layer with $Re_\theta = 1070$, as seen in Fig. 7 for locations in the buffer and logarithmic layers. The $P(\Omega_x, \Omega_y)$ JPDFs are plotted in (a), where the contours are

inclined toward the first and third quadrants, i.e., the quadrants of like sign vorticity components. The preferred orientation is even more evident in (b) where the covariance integrand $\Omega_x \Omega_y P(\Omega_x, \Omega_y)$ is plotted. The peak values in the first and third quadrants of the covariance integrand plots at each of the locations in the flow can be used to determine the orientation of the vortex lines that most contribute to the vorticity covariance,

$$\overline{\Omega_x \Omega_y} = \int_{-\infty}^{+\infty} \Omega_x \Omega_y P(\Omega_x, \Omega_y) d\Omega_x d\Omega_y. \quad (2)$$

The orientations, projected on the orthogonal coordinate planes from plots of all three vorticity covariance integrands at the three y^+ locations, are shown in Fig. 8 by Ong and Wallace.²⁸

Using dual plane PIV data from a turbulent boundary layer experiment at $Re_\theta = 2800$, as schematically illustrated in Fig. 9, Ganapathisubramani *et al.*³² observed the same preferential orientation of the vorticity vector projection on the streamwise (x - z) plane both from PDFs of the orientation angles and from the Ω_x - Ω_z covariance integrands, obtained further from the wall than the Ong and Wallace²⁸ data and seen in Fig. 10. Note that their coordinate system has z as the wall-normal direction, and y as the spanwise direction, i.e., the inverse of that used in this paper.

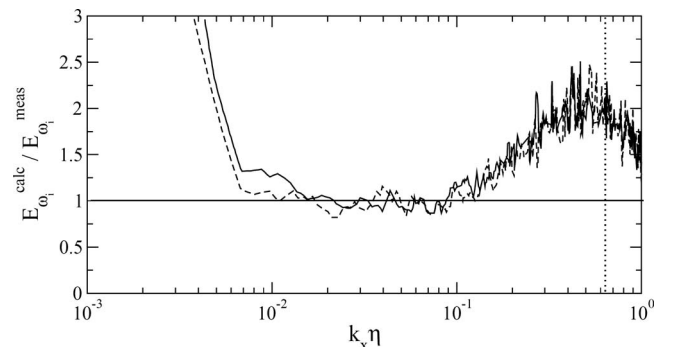


FIG. 13. Distributions of the ratios of wall normal and spanwise vorticity spectra calculated from Eq. (3) to their measured values (—) $i=y$; (---) $i=z$. Vertical dotted line indicates scale of the probe. Reprinted from Wallace and Ong (Ref. 34). Copyright © 2008 by the American Institute of Physics.

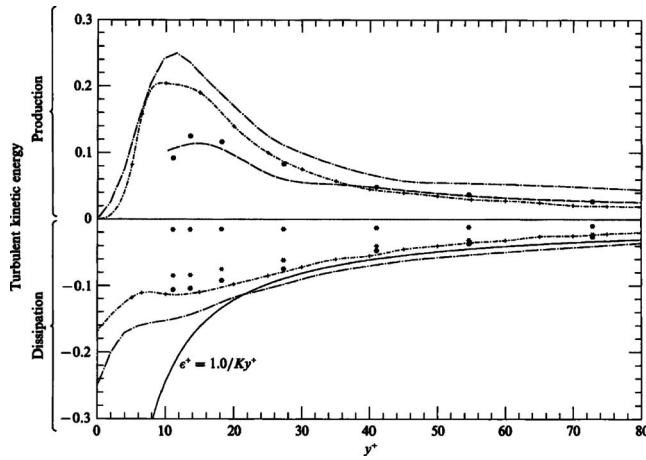


FIG. 14. Distribution of turbulent production and dissipation rates in wall bounded turbulent flows. (---) Kim *et al.* (Ref. 14), (- · - ·) Spalart (Ref. 27), (—) Wei and Willmarth (Ref. 35), (●) nine-sensor probe measurements in a turbulent boundary layer; other symbols are “*” homogeneous and “★” isotropic estimates. From Balint *et al.* (Ref. 29). Copyright © 1991 by Cambridge University Press. Reprinted with the permission of Cambridge University Press.

One of the interesting and important questions about vorticity component fields is whether or not they exhibit local isotropy characteristics at high wavenumbers. This question has been addressed using DNS by Kim and Antonia³³ and by Wallace and Ong³⁴ using the 12-sensor hot-wire probe shown in Fig. 11. One-dimensional k_x vorticity component spectra from both of these investigations are compared to the respective isotropic spectra determined from the DNS by Kim and Antonia³³ in Fig. 12.

The DNS spectra were computed at the centerline of a turbulent channel flow at $Re_\tau=395$. The experimental measurements were in the rough wall boundary layer of the interior test section roof of the NASA Ames 80×120 ft.² wind tunnel at $y/\delta=0.1$ and with $Re_\tau \approx 875$. In the inertial subrange, both the DNS and experimental spectra agree well with the isotropic spectra. For $k_x \eta > 0.2$ attenuation due to

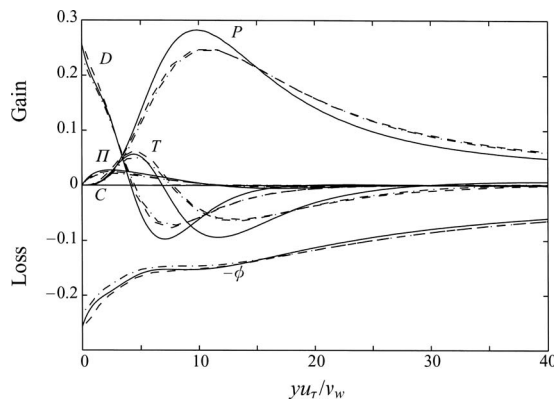


FIG. 15. Turbulent kinetic energy budget for a supersonic turbulent boundary layer. ϕ is the dissipation rate: (—) Guarini *et al.* (Ref. 36); (---) Spalart (Ref. 27) at $Re_\theta=1410$ and 670. From Guarini *et al.* (Ref. 36). Copyright © 2000 by Cambridge University Press. Reprinted with the permission of Cambridge University Press.

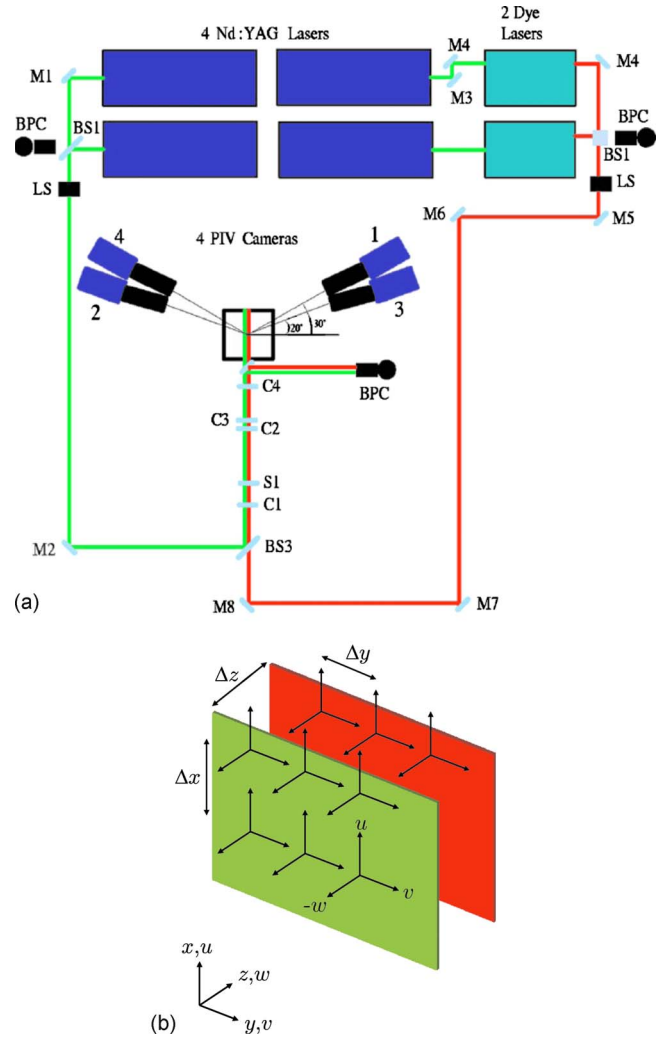


FIG. 16. (Color online) Sketch of frequency based dual plane PIV measurement system (above) and of velocity components measured in the front (green online) and back (red online) laser light planes spatially separated by distance Δz (below). Reprinted from Mullin and Dahm (Ref. 39). Copyright © 2006 by the American Institute of Physics.

spatial resolution is increasingly evident in the experimental spectra. The isotropic spectral relationship between the vorticity components

$$E_{\omega_y}(k_x) = E_{\omega_z}(k_x) = 1/2[E_{\omega_x}(k_x) - k_x dE_{\omega_x}(k_x)/dk_x], \quad (3)$$

analogous to that for the velocity components, can easily be shown; it also is implied because, like the velocity field, for incompressible flow the vorticity field is solenoidal. This relationship requires that, in a wavenumber range that is locally isotropic, the ratio of $E_{\omega_i}^{\text{calc}}$ calculated from Eq. (3) to the directly measured values $E_{\omega_i}^{\text{meas}}$, where $i=y$ or z , must be equal to unity. Figure 13 shows this ratio of the calculated cross-stream spectral density values of the vorticity components to their respective measured values. It is apparent that the vorticity field clearly tends toward isotropy near the beginning of the inertial subrange for the experimental data at $k_x \eta \approx 0.01$. The spanwise component approaches the isotropic value of unity at a slightly lower wavenumber than the

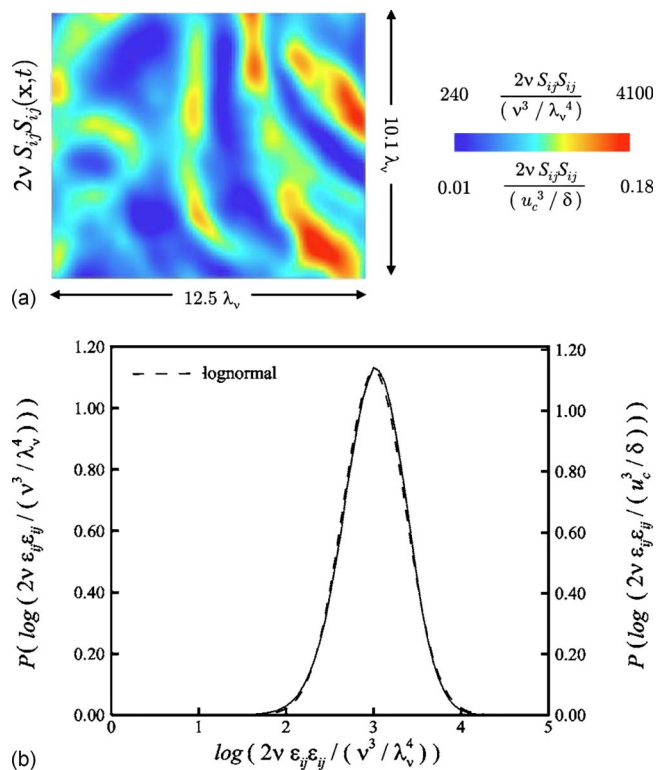


FIG. 17. (Color online) Typical turbulent kinetic energy dissipation rate field in a jet (above) and PDF of measured kinetic energy dissipation rate (below) at $Re_\lambda=45$ and zero mean shear rate. Reprinted from Mullin and Dahm (Ref. 39). Copyright © 2006 by the American Institute of Physics.

wall normal component. Departure from isotropy begins at $k_x \eta \approx 0.1$, which is at about the start of the dissipation range. This departure, a spatial resolution effect of the measurements, apparently results from the somewhat more rapid roll-off of the E_{ω_y} and E_{ω_z} spectra compared to the E_{ω_x} spectrum in the dissipation range.

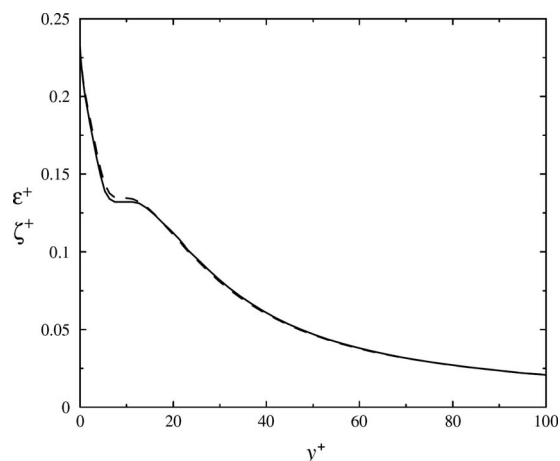


FIG. 18. Comparison of mean kinetic energy dissipation rate, (---) ε^+ and enstrophy (—) ζ^+ in channel flow DNS of Moser *et al.* (Ref. 41) at $Re_\tau = 590$. Reprinted from Bernard and Wallace (Ref. 40). Copyright © 2002 by John Wiley and Sons.

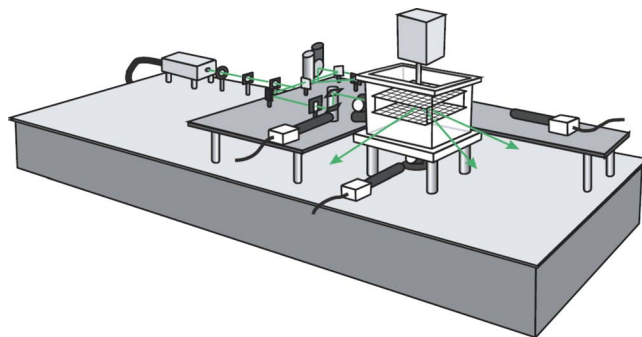


FIG. 19. (Color online) Sketch of three-dimensional microscopic PIV system of Zeff *et al.* (Ref. 42 by permission).

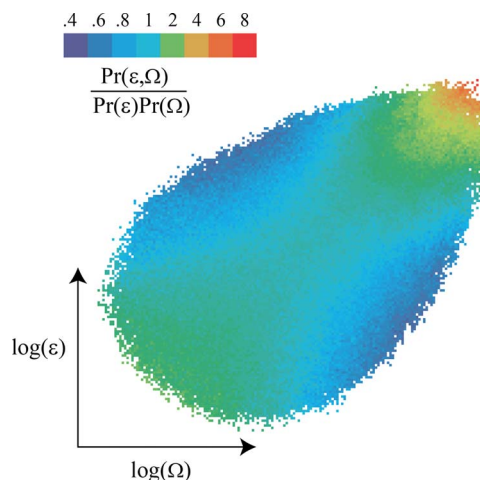


FIG. 20. (Color online) JPDP of kinetic energy dissipation rate and enstrophy in turbulent grid flow. Reprinted from Zeff *et al.* (Ref. 42). Copyright © 2003 by Nature.

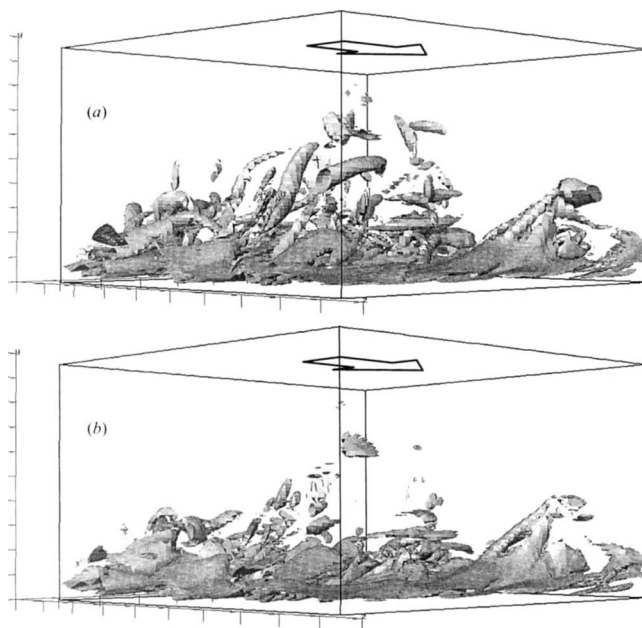


FIG. 21. Comparison of contours of constant (a) enstrophy and (b) dissipation rate in the channel flow DNS of Kim *et al.* (Ref. 13). From Blackburn (Ref. 43). Copyright © 1976 by Cambridge University Press. Reprinted with the permission of Cambridge University Press.

B. Dissipation rate

The turbulent kinetic energy dissipation rate is defined as

$$\varepsilon = \nu \left[\overline{\left(\frac{\partial u_i}{\partial x_j} \right)^2} + \overline{\frac{\partial u_i}{\partial x_j} \frac{\partial u_j}{\partial x_i}} \right], \quad (4)$$

where ν is the kinematic viscosity and represents a loss of energy to heat. Figure 14 shows the distributions of the production and dissipation rates from the nine-sensor probe experiment of Balint *et al.*²⁹ They are compared to the distributions of these properties obtained from the DNS studies of Kim *et al.*¹⁴ and Spalart.²⁷ Also shown are the approximate dissipation rate distributions obtained from the experiment by neglecting the inhomogeneous term in Eq. (4) and by assuming isotropy. The isotropic assumption has often previously been used to approximate the dissipation rate before means of determining the full dissipation rate were available. This assumption clearly leads to severely underestimated values near the wall, as is evident in the figure.

More recently, the dissipation rate distribution in a Mach 2.5 supersonic turbulent boundary layer with an adiabatic wall boundary condition has been calculated from a DNS at $Re_\theta = 1577$ by Guarini *et al.*³⁶ This distribution is shown as part of the turbulent kinetic energy balance distribution in Fig. 15 where it is compared to the distributions from the incompressible DNS simulations at two Reynolds numbers by Spalart.²⁷

Loucks³⁷ has measured the full dissipation rate for $\xi = y/\theta$ across a mixing layer with $Re_\theta = 1792$ from an experiment with a 12-sensor probe. Folz³⁸ compared these term by term contributions to the dissipation rate for a laboratory boundary layer at $Re_\theta = 1070$ and for the atmospheric surface layer in a field experiment under near neutral stability conditions with $Re_\theta = O(10^6)$. Both sets of measurements were made with 12-sensor probes with approximately the same spatial resolution.

Mullin and Dahm³⁹ have made measurements of the total dissipation rate in the far field of a self-similar turbulent jet at $Re_\lambda = 45$ and 113 and at two local mean shear rates. They used the two-plane stereo-PIV system schematically illustrated in Fig. 16. The instantaneous plane of their data shown in Fig. 17 illustrates how spatially intermittent the dissipation rate is. The figure also shows its PDF which is nearly log normal.

III. JOINT VELOCITY GRADIENT BASED TURBULENCE PROPERTIES

A. Dissipation rate and enstrophy

The exact relationship between the dissipation rate and enstrophy for turbulence that is homogeneous in the streamwise and spanwise directions and inhomogeneous in the cross-stream direction is $\varepsilon = \zeta + \partial^2(v^2)/\partial y^2$, where the enstrophy ζ is the sum of the vorticity component variances. Temporally developing free shear layer and channel flows are of this type. The second term on the right-hand side is obviously zero for turbulence homogeneous in all three coordinate directions. Bernard and Wallace⁴⁰ have compared in

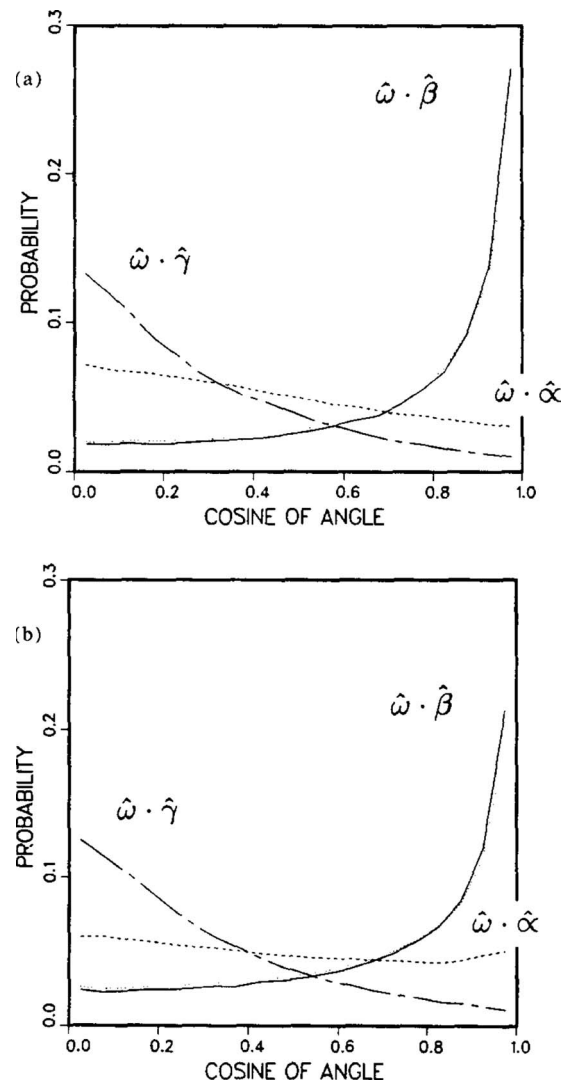


FIG. 22. Preferred alignment of the vorticity vector with the eigenvector associated with the intermediate eigenvalue β of the rate-of-strain tensor from (a) DNS of homogeneous turbulent shear flow (Ref. 16) and (b) isotropic turbulence (Ref. 10). α and γ are the extensional and compressive eigenvalues. Reprinted from Ashurst *et al.* (Ref. 17). Copyright © 1987 by the American Institute of Physics.

Fig. 18 the distributions of mean dissipation rate ε^+ and enstrophy ζ^+ normalized with wall variables, using the channel flow DNS of Moser *et al.*⁴¹ at $Re_\tau = 590$. Throughout the channel it is obvious that enstrophy is a good surrogate for the dissipation rate, indicating that the inhomogeneous term is negligible.

Zeff *et al.*⁴² used a three camera microscopic PIV technique, illustrated in Fig. 19, to measure the velocity gradient tensor and to compute from it the enstrophy and dissipation rate in a turbulent grid flow. The JPDP of their measurements of these properties is shown in Fig. 20. The close correspondence between enstrophy and dissipation rate is visually evident in the plot of surfaces of constant values of these two properties from the channel flow DNS of Kim *et al.*¹⁴ by Blackburn *et al.*⁴³ shown in Fig. 21.

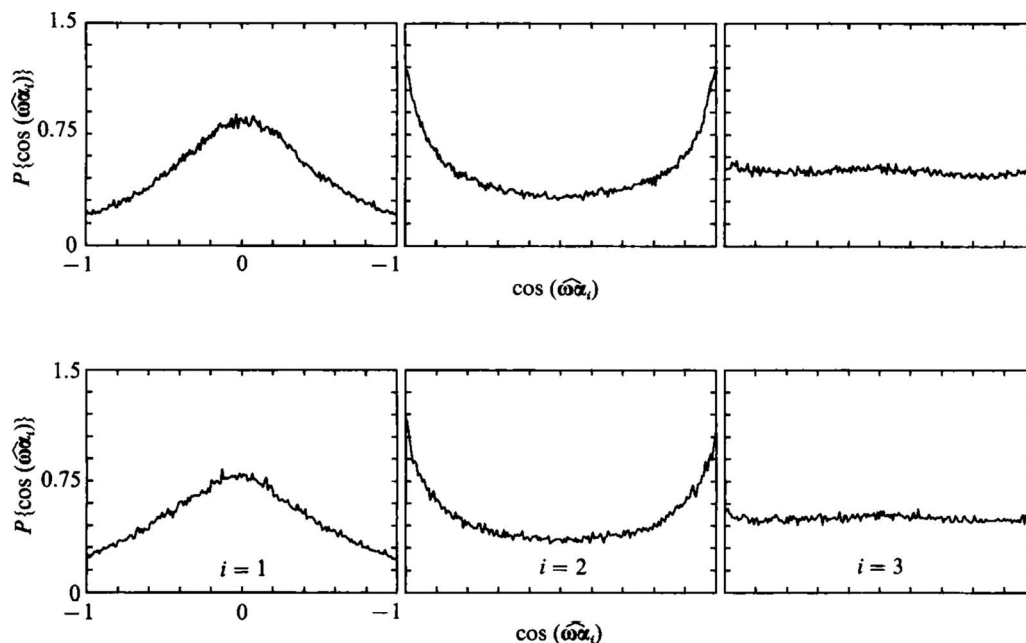


FIG. 23. Preferred alignment of the vorticity vector with the eigenvector associated with the intermediate eigenvalue α_2 of the rate-of-strain tensor measured in turbulent grid flow (above) and in a turbulent boundary layer (below). α_1 and α_3 are the compressive and extensional eigenvalues. From Tsinober *et al.* (Ref. 23). Copyright © 1992 by Cambridge University Press. Reprinted with the permission of Cambridge University Press.

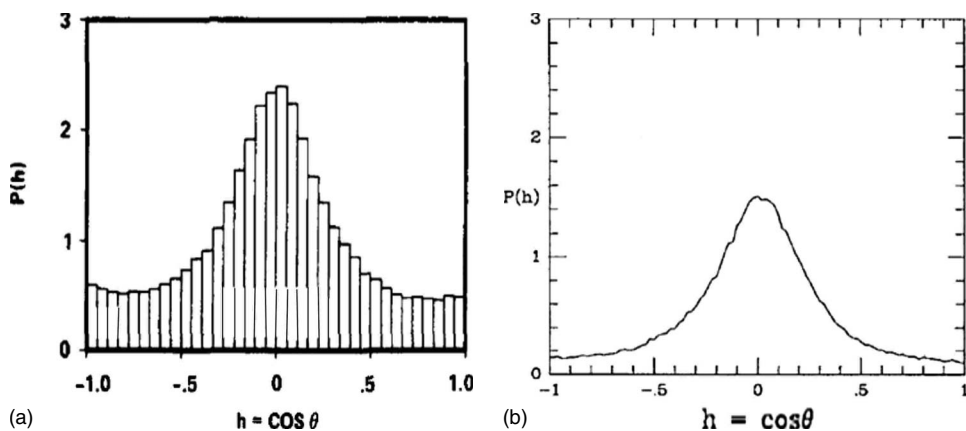


FIG. 24. PDF of relative helicity density at $y^+=19.2$ in a DNS channel flow (left) and at $y^+=18.3$ in an experimental boundary layer (right). Reprinted from Rogers and Moin [(Ref. 47), copyright © 1987 by the American Institute of Physics] and Wallace *et al.* [(Ref. 48), copyright © 1992 by the American Institute of Physics].

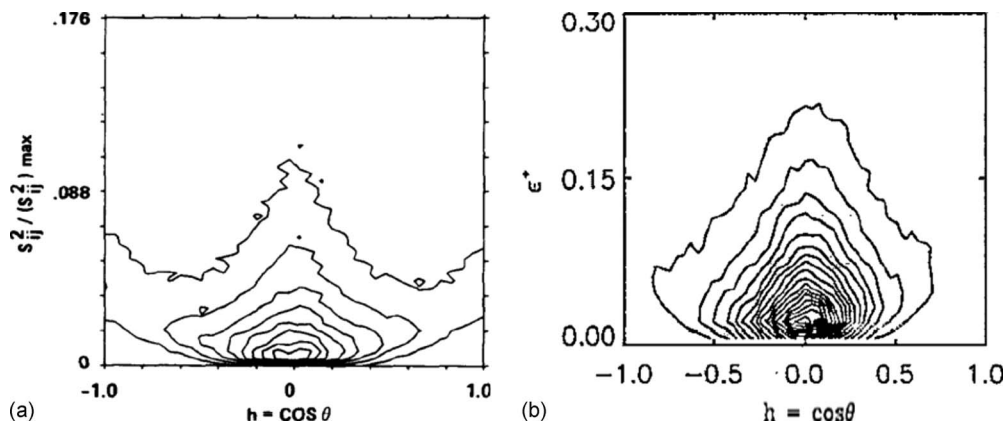


FIG. 25. JPDF of relative helicity density and kinetic energy dissipation rate at $y^+=19.2$ in a DNS channel flow (left) and $y^+=18.3$ in an experimental boundary layer (right). Reprinted from Rogers and Moin [(Ref. 47), copyright © 1987 by the American Institute of Physics] and Wallace *et al.* [(Ref. 48), copyright © 1992 by the American Institute of Physics].

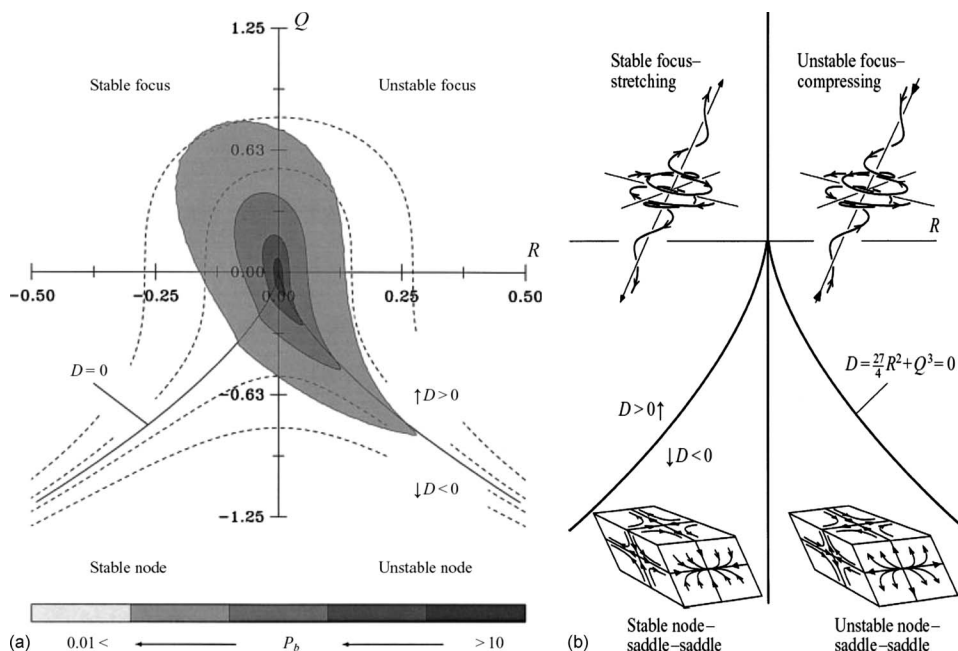


FIG. 26. JPDF of the Q and R invariants of the velocity gradient tensor from the $Re_\theta=670$ boundary layer DNS of Spalart (Ref. 27) with data throughout the flow domain (left). Three-dimensional flow patterns associated with the regions of the Q - R plane that are separated by the zero discriminant of the velocity gradient tensor, $D=0$ (right). From Chacin and Cantwell (Ref. 49). Copyright © 2000 by Cambridge University Press. Reprinted with the permission of Cambridge University Press.

B. Alignment of vorticity vector and eigenvectors of the strain-rate tensor

In the 20 years since the full velocity gradient tensor has been accessible, it has frequently been noted that a seemingly universal property of turbulence is the preferred alignment of the vorticity vector with the eigenvector associated with the intermediate eigenvalue of the rate-of-strain tensor β (or α_2 in Fig. 23), and that β is most often positive (extensional). This was first observed by Ashurst *et al.*¹⁷ using DNS of both isotropic turbulence¹⁰ at $Re_\lambda=83$ and homogeneous turbulent shear flow,¹⁶ as seen in Fig. 22 where PDFs of the cosine of the angle between the vorticity vector and eigenvectors of the rate-of-strain tensor are plotted. They also observed from this plot that the vorticity vector is least likely to align with the eigenvector associated with the most compressive eigenvalue γ (or α_1 in Fig. 23), i.e., that they are most probably orthogonal, and that there is almost no correlation with α (or α_3 in Fig. 23). This preferential alignment subsequently was experimentally confirmed by Tsinober *et al.*²³ using a 12-sensor probe in turbulent grid and boundary layer flows, as seen in Fig. 23, by Honkan and Andreopoulos²¹ with their nine-sensor hot-wire probe in a turbulent boundary layer, by Kholmyanski *et al.*²⁵ and by Gulitski *et al.*²⁶ in the atmospheric surface layer at $Re_\lambda=10^4$ and by Mullin and Dahm³⁹ with their dual plane PIV experiment in a turbulent jet. It has also been confirmed in many DNS investigations, including the DNS of isotropic flow at $Re_\lambda=150$ by Chevillard *et al.*,⁴⁴ who have modeled the velocity gradient tensor A_{ij} along Lagrangian trajectories with closures for the pressure Hessian and viscous Laplacian. Their model captures the preferred alignment quite well when compared to their DNS.

Ashurst *et al.*¹⁷ explained these alignment properties of the vorticity vector and the eigenvectors of the strain-rate

tensor with an argument based on the conservation of angular momentum. Jiménez⁴⁵ has explained this phenomenon with a simple kinematic argument showing that, for a vortex tube which is essentially two-dimensional and whose maximum vorticity is large compared to its surroundings, the strain-rate field induced by it is normal to the vortex and dominates the strain-rate tensor. Thus, the eigenvalue associated with the residual, intermediate eigenvalue is aligned with the vortex tube and stretches or compresses it.

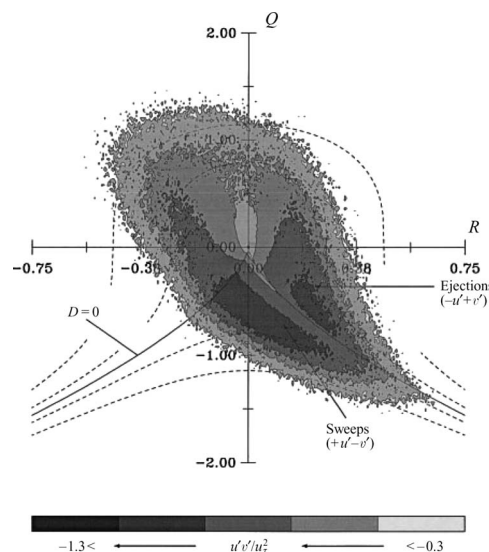


FIG. 27. Time-averaged Q_2 (ejection: $-u, +v$) and Q_4 (sweep: $+u, -v$) Reynolds shear stress events associated with the incompressible flow patterns of Fig. 27. From Chacin and Cantwell (Ref. 49). Copyright © 2000 by Cambridge University Press. Reprinted with the permission of Cambridge University Press.

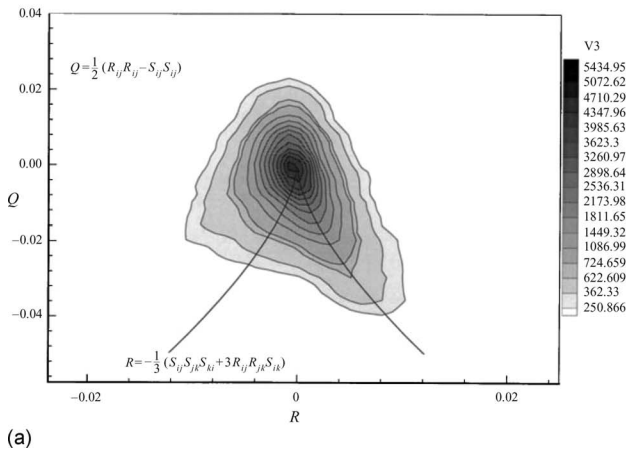


FIG. 28. JPDF of the Q and R invariants of the velocity gradient tensor from a $Re_\theta=2790$ boundary layer experiment at $y^+=12.5$ (left). Photograph of nine-sensor hot-wire probe (right). From Andreopoulos and Honkan (Ref. 52). Copyright © 2001 by Cambridge University Press. Reprinted with the permission of Cambridge University Press.

C. Helicity density alignment of the vorticity and velocity vectors

Moffatt⁴⁶ speculated that turbulence might be described as steady solutions to the Euler equations about which unsteady solutions evolve. In the subdomains where the steady Euler solutions exist, which he thought objectively could be considered coherent structures, the relative helicity density, $h = \mathbf{U} \cdot \mathbf{V} / |\mathbf{U}| |\mathbf{V}| = \cos \theta$, where $\cos \theta$ is the angle between the vorticity and velocity vectors, should be maximal at ± 1 . He expected that the flow regions between these subdomains might be vortex sheets that could be the principal locus of viscous dissipation. Thus, he argued, high relative helicity density may be correlated with low kinetic energy dissipation rate and vice versa.

Rogers and Moin⁴⁷ examined the DNS of several homogeneous and inhomogeneous flows to test these ideas. They pointed out that the variance of h is 0.333 for two isotropic vector fields that are uncorrelated, and that the PDFs are flat for this special case for all values of h . Wallace *et al.*⁴⁸ also tested these ideas using turbulent grid flow and boundary and mixing layer data obtained with a nine-sensor hot-wire probe. Figure 24 shows the PDF of h as a function of h for $y^+=19.2$ in the DNS channel flow and $y^+=18.3$ in the experimental boundary layer. In both cases, $P(h)$ has a strong peak, at $h=0$, indicating that the highest probability is for the two vectors not to be aligned. Figure 25 shows the JPDF of dissipation rate and helicity density for these two flows. The peaks of these JPDFs are at $h=0$, but also are at very low values of the dissipation rate. In fact, throughout the flow domains there is a low probability of large instantaneous dissipation rate and small ($h \approx 0$) relative helicity density occurring simultaneously except in shear flow regions where dissipation rate amplitudes are small compared to the largest values in the flow domain.

D. Invariants Q and R of the velocity gradient tensor

The characteristic equation for the velocity gradient tensor A_{ij} is $\lambda^3 + P\lambda^2 + Q\lambda + R = 0$, where the invariants of the tensor are $P = -S_{ii} = 0$ for incompressible flow, $Q = \frac{1}{2}(-S_{ij}S_{ij} + R_{ij}R_{ij})$, and $R = -\frac{1}{3}(S_{ij}S_{jk}S_{ki} + 3R_{ij}R_{jk}S_{ki})$. Here S_{ij} and R_{ij} are the strain-rate and rotation rate tensors as defined earlier. Chacin and Cantwell⁴⁹ have plotted the JPDF of Q

and R for the $Re_\theta=670$ boundary layer data of Spalart²⁷ as seen in Fig. 26. Also shown in the figure is the summary of three-dimensional flow patterns associated with the regions of the Q - R plane from Soria *et al.*⁵⁰ that are separated by the Vieillefosse line, i.e., the locus of zero values of the cubic discriminant of A_{ij} for incompressible flow, $D = \frac{27}{4}R^2 + Q^3$. Chacin and Cantwell⁴⁹ have computed the distribution of the time-averaged (over the complete flow domain) Reynolds shear stress associated with these flow patterns. The shear stress is dominated by the Q2 (ejection: $-u, +v$) and Q4 (sweep: $+u, -v$) quadrants of the u - v momentum flux plane (see Wallace *et al.*⁵¹) which are superimposed on the time-averaged Q - R plane in Fig. 27. This shows that the unstable focus compressing pattern is mostly associated with Q2, and the unstable node-saddle-saddle pattern with Q4 momentum flux.

Remarkably, the teardrop shaped JPDF of Q and R appears to be a universal characteristic of turbulence because it has been observed in a wide variety of shear flows as well as in isotropic turbulence, both from DNS and experiments. Figure 28 shows this same teardrop shaped distribution obtained experimentally by Andreopoulos and Honkan⁵² in a turbulent boundary layer at $y^+=12.5$ with their nine-sensor probe, also shown in the figure. Recently Gulitski *et al.*²⁶

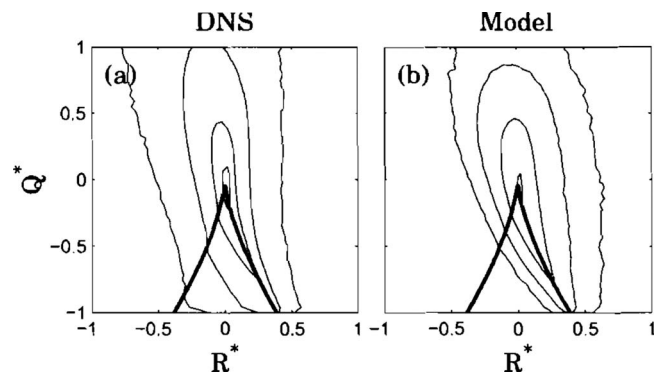


FIG. 29. JPDF of the Q and R invariants of the velocity gradient tensor from (a) DNS of isotropic turbulence with $Re_\lambda=150$ and (b) model with closures of the pressure Hessian and viscous Laplacian. The thick line represents the zero-discriminant (Vieillefosse) line $D = \frac{27}{4}R^2 + Q^3 = 0$. Reprinted from Chevillard *et al.* (Ref. 44). Copyright © 2008 by the American Institute of Physics.

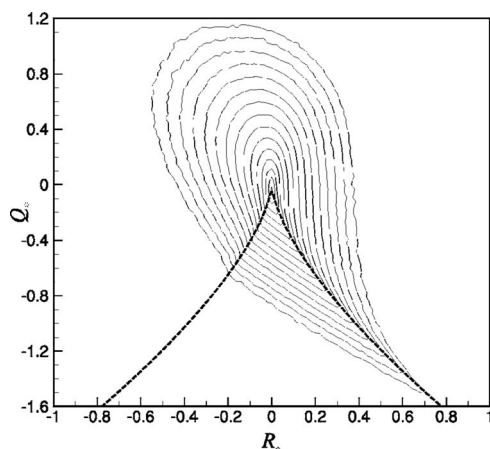


FIG. 30. JPDF of the Q and R invariants of the velocity gradient tensor computed from a synthesized non-Gaussian turbulent vector field. Reprinted from Rosales and Meneveau (Ref. 53). Copyright © 2006 by the American Institute of Physics.

obtained the same shape JPDF in their atmospheric surface layer experiment. The model of Chevillard *et al.*⁴⁴ of the velocity gradient tensor with closures of the pressure Hessian and the viscous Laplacian yields an excellent representation of this teardrop shaped distribution, as shown in Fig. 29, where their model distribution is compared to their DNS result. Equally remarkably, Rosales and Meneveau⁵³ showed that this teardrop shaped JPDF (Fig. 30) can be produced from synthetic vector fields, generated by deforming an initial Gaussian field from random-phase Fourier modes, as surrogates for turbulent velocity fields. The deformation is accomplished by moving particles of a sequence of low-pass filtered fields at their fixed velocities over scale dependent time intervals, interpolating on a regular grid and imposing the divergence free condition. Several other velocity and velocity gradient properties, such as the preferred alignment of the vorticity vector with the eigenvector associated with the intermediate eigenvalue of the rate-of-strain tensor, described above, are also observed. Differences from real turbulence fields created with DNS are only observed in the detailed

measures of properties of intense small scale vortex tubes (see below) which do not occur in the synthetic turbulence.

IV. STRUCTURE

It was a strong hope of turbulence researchers 40 years ago that access to properties of turbulence, such as vorticity, by way of the velocity gradient tensor would lead to much more clarity about the structural organization of turbulent flows and how this is related to the processes of heat, mass, and momentum transport. This hope has been partially realized.

In their 240³ DNS of isotropic turbulence at $Re_\lambda=150$, Vincent and Meneguzzi⁵⁴ observed that the vorticity field is organized in thin elongated tubes with thicknesses of the order of a few dissipation scales, confirming earlier results.^{10,55,56} These structures, commonly known as “turbulence worms,” are readily seen in Fig. 31 where the vorticity field is represented by vectors of length proportional to vorticity amplitude at each grid point that exceed a specified amplitude threshold. The wormlike structures are made up of the clustering of these vectors. The velocity vector field in a plane perpendicular to one of these structures, also shown in the figure, clearly shows the strong rotation of the vortex compared to its surroundings. In Fig. 32 two eigenvectors of the rate-of-strain tensor are shown with these vorticity vectors. The negative (compressive) eigenvector α_1 is often perpendicular to the vorticity vector, as seen on the left of the figure, and the intermediate eigenvector α_2 is frequently well aligned with the vorticity vector, as seen on the right, consistent with the results cited above. As for the vorticity vector, only eigenvectors exceeding a chosen amplitude threshold are shown.

For homogeneous shear flow, the vorticity lines plotted by Rogers and Moin¹⁶ in Fig. 33 suggest that this flow is organized in looplike structures; the vorticity component boundary layer JPDF study of Ong and Wallace²⁸ suggested a similar vortex filament structure, as sketched in Fig. 34.

However, the vortex lines configured in such shapes do not necessarily indicate the presence of coherent vortices. A

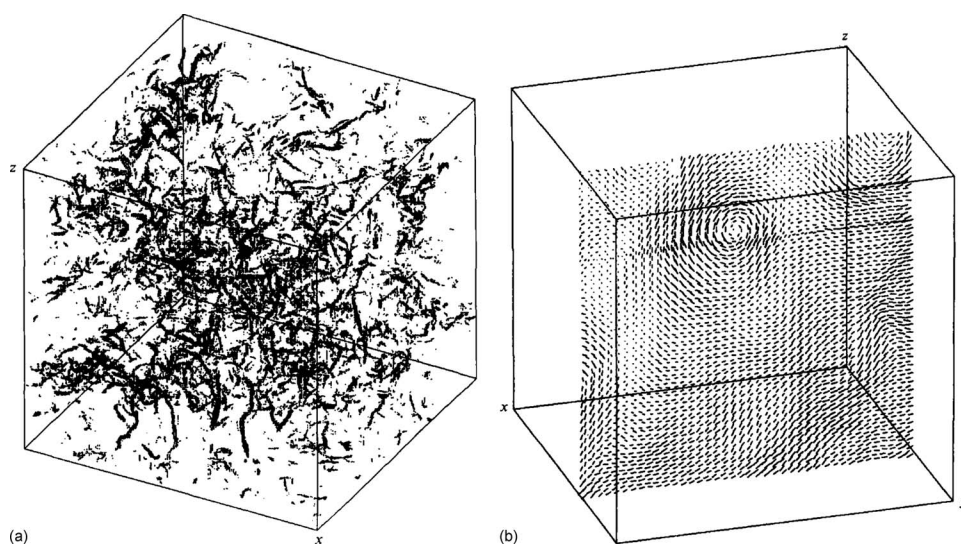


FIG. 31. Turbulent “worms” in isotropic turbulence at $Re_\lambda=150$: vorticity field represented by vector lengths proportional to amplitude at each node (left) and projection of velocity field perpendicular to a vorticity tube worm (right). From Vincent and Meneguzzi (Ref. 54). Copyright © 1991 by Cambridge University Press. Reprinted with the permission of Cambridge University Press.

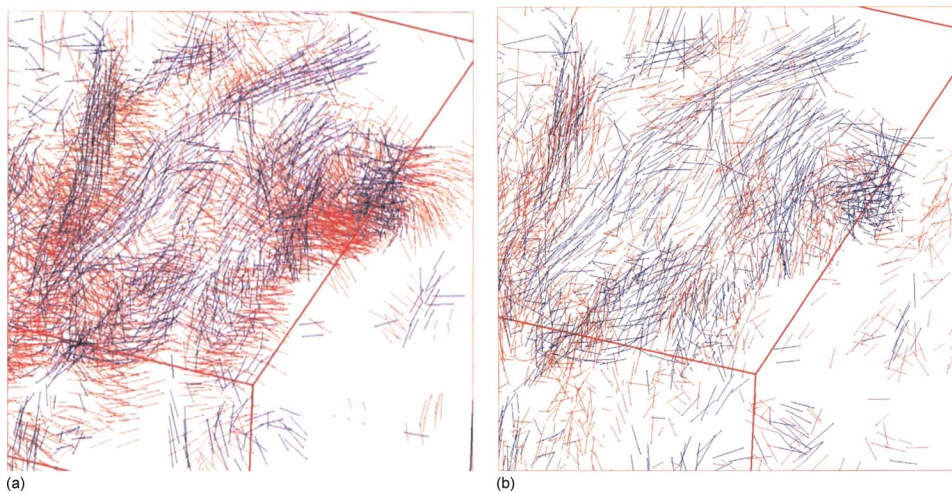


FIG. 32. (Color online) Eigenvectors of the rate of strain tensor “light gray” (red online): α_1 (compressive, left) and α_2 (intermediate, right) and vorticity vectors “dark gray” (blue online). From Vincent and Meneguzzi (Ref. 54). Copyright © 1991 by Cambridge University Press. Reprinted with the permission of Cambridge University Press.

great deal of effort has been devoted to developing objective criteria for identifying vortices in turbulence. Chakraborty *et al.*⁵⁷ have compared the methods that use properties of the velocity gradient tensor by identifying vortices in the forced 256^3 isotropic turbulence DNS of Langford and Moser⁵⁸ with $Re_\lambda = 164$. The methods compared were the following.

- (1) The Q criterion of Hunt *et al.*⁵⁹ which identifies vortices as regions of positive second invariant of A_{ij} combined with pressure in the identified vortex required to be lower than ambient.
- (2) The criterion of Jeong and Hussain⁶⁰ which defines the cores of vortices as local pressure minima in chosen planes identified as connected regions with two positive eigenvalues of the pressure Hessian (shown by Chakraborty *et al.*⁵⁷ to be equivalent to requiring that the intermediate eigenvalue of Q , $\lambda_2 < 0$).
- (3) The criterion of Chong *et al.*⁶¹ which defines the cores of vortices to be the regions where A_{ij} has complex eigenvalues, which is equivalent to requiring that the discriminant of the characteristic equation of A_{ij} , Δ (or D) > 0 .
- (4) The swirling strength criterion λ_{ci} of Zhou *et al.*⁶² which is based on the Δ (or D) criterion and identifies vortices using the imaginary part of the complex conjugate eigenvalue of A_{ij} .
- (5) A special case λ_2 criterion when the eigenbasis vectors of A_{ij} are orthonormal.

The swirling strength criterion not only identifies vortices but also determines their strength and local plane of swirling. Figure 35 shows the vortex worms in this isotropic flow as identified by the different criteria using thresholds that are chosen in relation to the λ_{ci} threshold. There is a high degree of visual correspondence between the vortices identified by all the criteria, and this is confirmed in the table which shows the percentage of volume overlap between the flow regions occupied by the identified vortices.

Figure 36 shows the vortices identified by Ganapathisubramani *et al.*³² as isosurfaces of swirl strength⁶² using the Δ criterion in the channel flow DNS of Del Alamo *et al.*⁶³ The vortices are mostly inclined downstream, and numerous

looplike structures are evident. Similar vortical structures have been identified by Ferrante *et al.*⁶⁴ in a turbulent boundary layer DNS using the local pressure minimum λ_2 criterion of Jeong and Hussain.⁶⁰ These are shown in Fig. 37, and dynamically in the online version [video](#).

Zhou *et al.*⁶² studied the average evolution of such vortices and the formation of vortex clusters in a channel flow DNS, as shown in Fig. 38 where the vortices are identified by iso-surfaces of the square of the swirl strength. In (a) the primary vortex is extracted from the two-point spatial correlation of the velocity field by linear stochastic estimation given a Q2 ejection event vector. New vortices are generated upstream and also downstream and to the side of the primary vortex, as seen at the subsequent times [(b)–(d)]. These clusters of vortices are called packets.

Following the lead of the earlier study by Metcalfe *et al.*,¹⁵ Rogers and Moser⁶⁵ investigated the three-

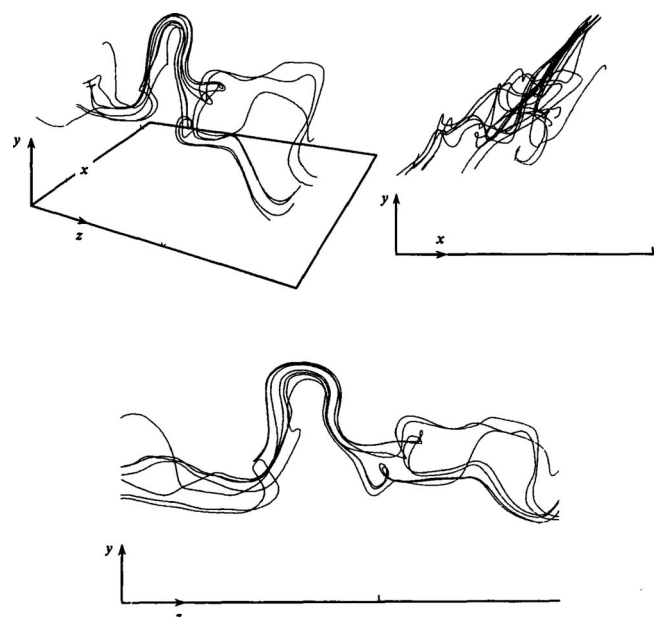


FIG. 33. Vortex lines in homogeneous turbulent shear flow DNS. From Rogers and Moin (Ref. 16). Copyright © 1987 by Cambridge University Press. Reprinted with the permission of Cambridge University Press.

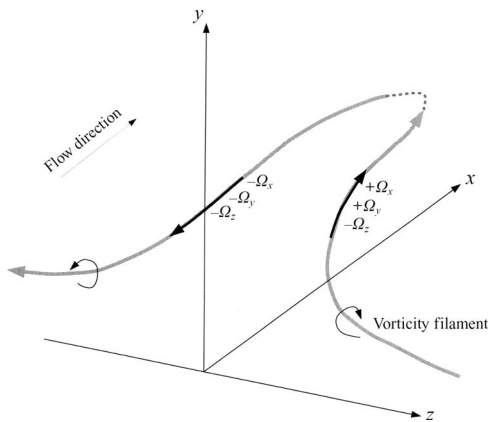


FIG. 34. Sketch of the inclined vorticity filaments (below). From Ong and Wallace (Ref. 28). Copyright © 1998 by Cambridge University Press. Reprinted with the permission of Cambridge University Press.

dimensional evolution of a temporally developing plane mixing layer, initiated by the Kelvin–Helmholtz rollup, into a structural configuration characterized by roller and rib vortices. In Fig. 39(a) surfaces of constant vorticity magnitude

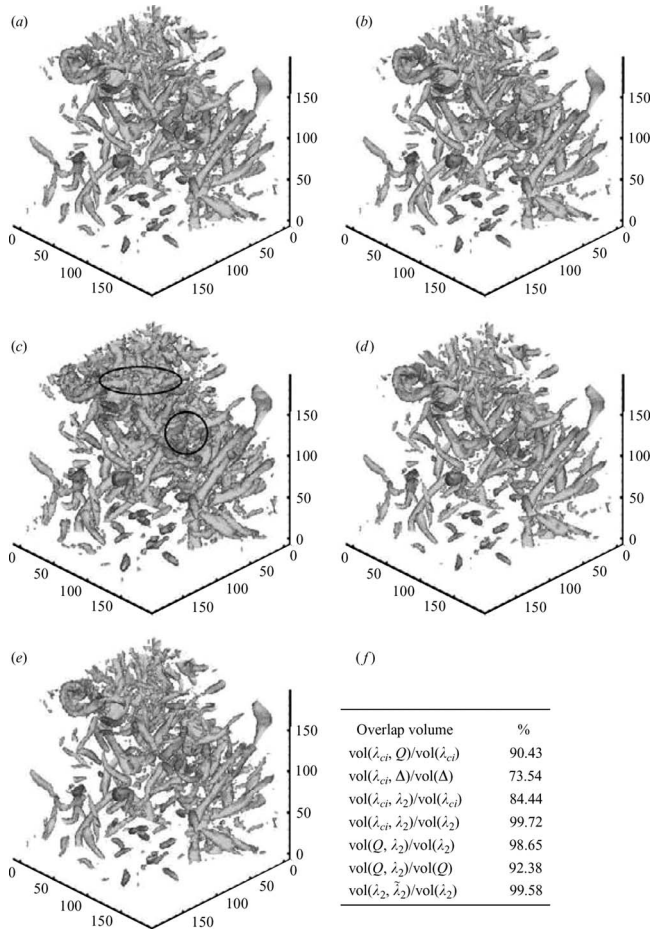


FIG. 35. Vortex worms in isotropic turbulence identified using various criteria based on velocity gradient tensor properties: (a) λ_{ci} , (b) Q , (c) Δ , (d) λ_2 , (e) special case λ_2 (see text). (f) Table indicates the volume percentage of overlap. From Chakraborty *et al.* (Ref. 57). Copyright © 2005 by Cambridge University Press. Reprinted with the permission of Cambridge University Press.

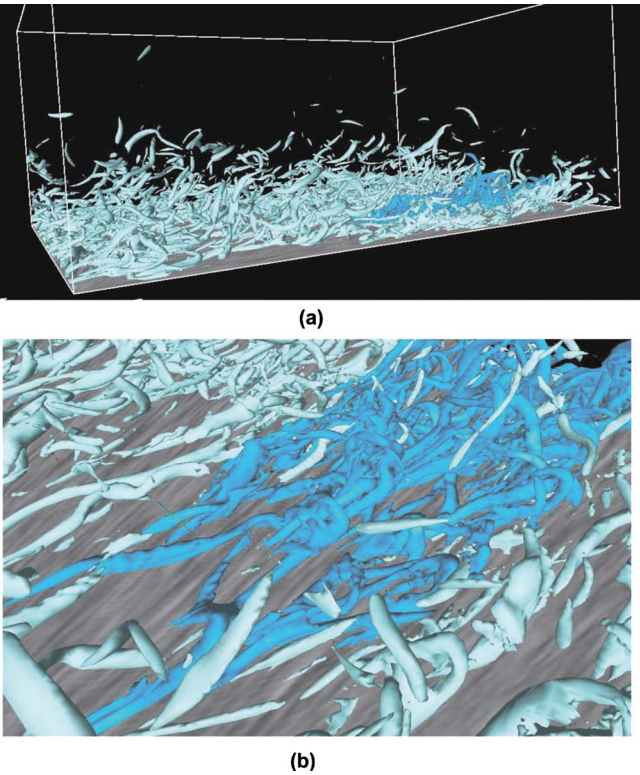


FIG. 36. (Color online) Vortices identified using the swirl strength criterion in the channel flow DNS of Del Alamo *et al.* (Ref. 63): (a) full computational domain, (b) zoomed view. Reprinted from Ganapathisubramani *et al.* (Ref. 32). Copyright © 2006 by the American Institute of Physics.

indicate the presence of the rib vortices primarily oriented in the streamwise plane. The vorticity lines in (b) show that the spanwise vorticity rolls up into corrugated roller vortices with vortex stretching creating strong spanwise vorticity in cup-shaped regions at the bends of the rollers. In (c) and (d) contours of ω_z indicate cross sections of rollers between ribs at two times.

These turbulent mixing layer rib and roller vortices are best seen in Fig. 40 visualized from a large eddy simulation of this flow by Comte *et al.*⁶⁶ The figure is a single frame, but the temporal evolution of these vortices can be seen in the online version [video](#).



FIG. 37. (Color online) Vortices identified using the pressure minimum λ_2 criterion (Ref. 60) in a turbulent boundary layer. Reprinted from Ferrante *et al.* (Ref. 64). Copyright © 2004 by the American Institute of Physics (enhanced online). [URL: <http://dx.doi.org/10.1063/1.3046290.1>]

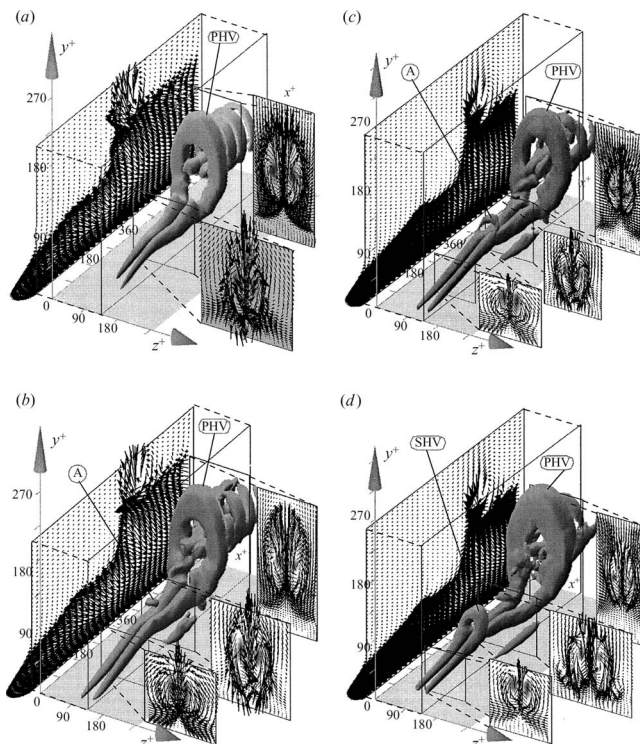


FIG. 38. Average evolution of vortices and the formation of vortex clusters [(a)–(d)] in channel flow DNS. PHV indicates primary hairpin vortex, SHV indicates secondary hairpin vortex, and A indicates spanwise hairpin arch. From Zhou *et al.* (Ref. 62). Copyright © 1999 by Cambridge University Press. Reprinted with the permission of Cambridge University Press.

In Fig. 41 phase averaged projections of velocity vectors on the streamwise plane of a plane mixing layer at $R_\theta = 1792$ is shown in a frame convecting with the midlevel velocity. These are from measurements by Loucks³⁷ with the 12-sensor probe in Fig. 11 and spaced across the layer at the locations of the horizontal lines of vectors. The measurements have been phased referenced to the passage of the

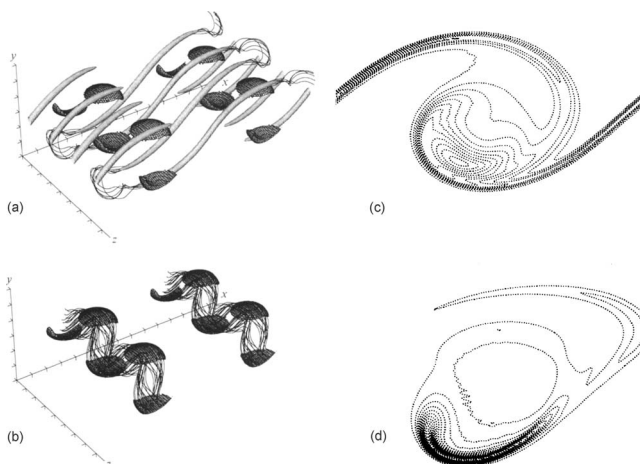


FIG. 39. Visualization in a temporally evolving turbulent two-stream mixing layer of (a) isosurfaces of vorticity magnitude, (b) vorticity lines, and [(c) and (d)] contours of ω_z indicating cross sections of roller vortices between rib vortices at two times. From Rogers and Moser (Ref. 65). Copyright © 1992 by Cambridge University Press. Reprinted with the permission of Cambridge University Press.

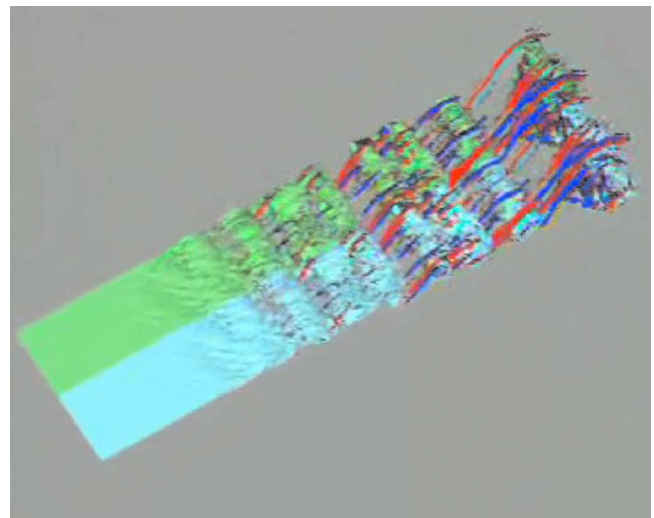


FIG. 40. (Color online) Visualization of turbulent rib and roller vortices in a two-stream mixing layer LES of Comte *et al.* (Ref. 66) by permission (enhanced online). [URL: <http://dx.doi.org/10.1063/1.3046290.2>]

roller vortices as detected by a single-sensor probe placed in the freestream above the layer. The 12-sensor probe provided a rich source of information about various properties of the turbulence, particularly those based on the velocity gradient tensor, all of which could also be phased averaged so that their spatial distribution with respect to the locations of the phase averaged roller vortices could be determined. In (b) the Reynolds shear stress contours are seen to peak at the periph-

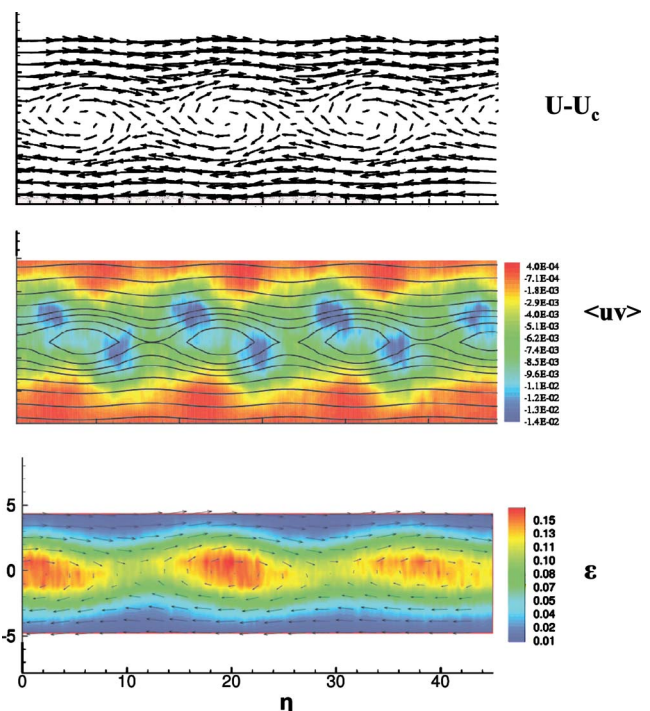


FIG. 41. (Color online) Phase averaged (top) projection of velocity vectors on the streamwise plane, (middle) Reynolds shear stress, and (bottom) kinetic energy dissipation rate, all phase referenced to the passage of the spanwise roller vortices in a two-stream turbulent plane mixing layer at $R_\theta = 1792$. Measurements made with 12-sensor probe shown in Fig. 11. From Loucks (Ref. 37) by permission.

eries of the roller vortex cores, above them downstream and below upstream. In (c) the turbulent dissipation rate is seen to peak within the cores of the vortices.

V. CONCLUSIONS

Over the past two decades great progress has been made in understanding many aspects of the kinematics and dynamics of a wide variety of turbulent flows as a result of access to the velocity gradient tensor. This great progress in understanding turbulence, in my view, shows that the oft stated idea that fluid mechanics is a “mature” field (in the sense of exhausted) is far from true. Our best days are ahead of us!

ACKNOWLEDGMENTS

First and foremost I am deeply indebted to my former students and later colleagues and good friends, Jean-Louis Balint and Petar Vukoslavčević, who, with great perseverance, developed with me the multisensor probes and data analysis algorithms that were used in the investigations from our laboratory that are cited in this paper. I am further indebted to my former graduate students: Alan Folz, Elefantis Kastrinakis, Rick Loucks, Ning Li, Lawrence Ong (later a postdoctoral associate), Seong-Ryong Park, Phuc Nguyen, and Bill Wassmann for the skill they showed in performing many of the experiments cited herein and for giving me the pleasure of working with them. I am also indebted to my colleagues Elias Balaras (who kindly helped me with the technical production of this paper), Peter Bernard, Ugo Piomelli, and Serge Simöens who have collaborated with me on many investigations that gave us insights about some of the turbulence phenomena described here. Finally, grant support over the years from NSF, DOE, NASA, and the CTR summer program is gratefully acknowledged.

¹S. J. Kline, W. C. Reynolds, F. A. Schraub, and P. W. Runstadler, “The structure of turbulent boundary layers,” *J. Fluid Mech.* **30**, 741 (1967).

²E. R. Corino and R. S. Brodkey, “A visual investigation of the wall region in turbulent flow,” *J. Fluid Mech.* **37**, 1 (1969).

³G. L. Brown and A. Roshko, “On density effects and large structure in turbulent mixing layers,” *J. Fluid Mech.* **64**, 775 (1974).

⁴J. H. Konrad, “An experimental investigation of mixing in two-dimensional turbulent shear flows with applications to diffusion-limited chemical reactions,” Ph.D. dissertation, California Institute of Technology, 1976.

⁵M. R. Head and P. Bandyopadhyay, “New aspects of turbulent boundary layer structure,” *J. Fluid Mech.* **107**, 297 (1981).

⁶J. M. Wallace, “On the structure of bounded turbulent shear flow: A personal view,” in *Developments in Theoretical and Applied Mechanics XI*, Proceedings of the 11th Southeastern Conference on Theoretical and Applied Mechanics, Huntsville, AL, April 8–9, 1982, edited by T. J. Chung and G. R. Karr, p. 509.

⁷J. Laufer, “New trends in experimental turbulence research,” *Annu. Rev. Fluid Mech.* **7**, 307 (1975).

⁸S. A. Orszag and G. S. Patterson, “Numerical simulation of three-dimensional homogeneous isotropic turbulence,” *Phys. Rev. Lett.* **28**, 76 (1972).

⁹R. S. Ragallo, “Numerical experiments in homogeneous turbulence,” NASA Report No. TM 81315, 1981.

¹⁰R. Kerr, “Higher-order derivative correlations and the alignment of small-scale structures in isotropic numerical turbulence,” *J. Fluid Mech.* **153**, 31 (1985).

¹¹J.-L. Balint, P. Vukoslavčević, and J. M. Wallace, “A study of the vortical structure of the turbulent boundary layers,” in *Advances in Turbulence*, edited by G. Comte-Bellot and J. Mathieu (Springer, New York, 1987), pp. 456–464.

¹²J.-L. Balint, “Contribution à l’étude de la structure tourbillonnaire d’une couche limite turbulente au moyen d’une sonde à neuf fils chauds mesurant le rotationnel,” Thèse de Docteur d’Etat ès Sciences, Université de Lyon, 1986.

¹³L. W. B. Browne, R. A. Antonia, and D. A. Shah, “Turbulent energy dissipation in a wake,” *J. Fluid Mech.* **179**, 307 (1987).

¹⁴J. Kim, P. Moin, and R. D. Moser, “Turbulence statistics in fully-developed channel flow at low Reynolds,” *J. Fluid Mech.* **177**, 133 (1987).

¹⁵R. W. Metcalfe, S. A. Orszag, M. E. Brachet, S. Menon, and J. J. Riley, “Secondary instability of a temporally growing mixing layer,” *J. Fluid Mech.* **184**, 207 (1987).

¹⁶M. M. Rogers and P. Moin, “The structure of the vorticity field in homogeneous turbulent flows,” *J. Fluid Mech.* **176**, 33 (1987).

¹⁷Wm. T. Ashurst, A. R. Kerstein, R. M. Kerr, and C. H. Gibson, “Alignment of vorticity and scalar gradient with strain rate in simulated Navier–Stokes turbulence,” *Phys. Fluids* **30**, 2343 (1987).

¹⁸P. Vukoslavčević, J.-L. Balint, and J. M. Wallace, “The velocity and vorticity vector fields of a turbulent boundary layer. Part 1. Simultaneous measurement by hot-wire anemometry,” *J. Fluid Mech.* **228**, 25 (1991).

¹⁹G. I. Taylor, “Production and dissipation of vorticity in a turbulent fluid,” *Proc. R. Soc. London, Ser. A* **164**, 15 (1938).

²⁰U. Piomelli, J. L. Balint, and J. M. Wallace, “On the validity of Taylor’s hypothesis for wall-bounded flows,” *Phys. Fluids A* **1**, 609 (1989).

²¹A. Honkan and Y. Andreopoulos, “Vorticity, strain-rate and dissipation characteristics in the near-wall region of turbulent boundary layers,” *J. Fluid Mech.* **350**, 29 (1997).

²²P. Vukoslavčević and J. M. Wallace, “Measurements of the vorticity vector and other velocity gradient tensor-based turbulence properties,” in *Handbook of Experimental Fluid Mechanics*, edited by C. Tropea, A. L. Yarin, and J. F. Foss (Springer, New York, 2007), pp. 408–429.

²³A. Tsinober, E. Kit, and T. Dracos, “Experimental investigation of the field of velocity gradients in turbulent flows,” *J. Fluid Mech.* **242**, 169 (1992).

²⁴P. Vukoslavčević and J. M. Wallace, “A 12-sensor hot-wire probe to measure the velocity and vorticity vectors in turbulent flows,” *Meas. Sci. Technol.* **7**, 1451 (1996).

²⁵M. Kholmyansky, A. Tsinober, and S. Yorish, “Velocity derivatives in the atmospheric surface layer at $Re_\lambda = 10^4$,” *Phys. Fluids* **13**, 311 (2001).

²⁶G. Gulitski, M. Kholmyansky, W. Kinzelbach, B. Lüthi, A. Tsinober, and S. Yorish, “Velocity and temperature derivatives in high Reynolds number turbulent flows in the atmospheric surface layer. Part I. Facilities, methods and some general results,” *J. Fluid Mech.* **589**, 57 (2007).

²⁷P. R. Spalart, “Direct simulation of a turbulent boundary layer up to $Re_\theta = 1410$,” *J. Fluid Mech.* **187**, 61 (1988).

²⁸L. Ong and J. M. Wallace, “Joint probability density analysis of the structure and dynamics of the vorticity field of a turbulent boundary layer,” *J. Fluid Mech.* **367**, 291 (1998).

²⁹J. L. Balint, P. Vukoslavčević, and J. M. Wallace, “The velocity and vorticity vector fields of a turbulent boundary layer. Part 2. Statistical properties,” *J. Fluid Mech.* **228**, 53 (1991).

³⁰E. G. Kastrinakis and H. Eckelmann, “Measurements of streamwise vorticity fluctuations in a turbulent channel flow,” *J. Fluid Mech.* **137**, 165 (1991).

³¹J. Klewicki, “On the interactions between the inner and outer motions in turbulent boundary layers,” Ph.D. dissertation, Michigan State University, 1989.

³²B. Ganapathisubramani, E. K. Longmire, and I. Marusic, “Experimental investigation of vortex properties in a turbulent boundary layer,” *Phys. Fluids* **18**, 055105 (2006).

³³J. Kim and R. A. Antonia, “Isotropy of the small scales of turbulence at low Reynolds number,” *J. Fluid Mech.* **251**, 219 (1993).

³⁴J. M. Wallace and L. Ong, “Local isotropy of the velocity and vorticity fields in a boundary layer at high Reynolds number,” *Phys. Fluids* **20**, 101506 (2008).

³⁵T. Wei and W. W. Willmarth, “Reynolds number effects on the small scale structure of a turbulent channel flow,” *J. Fluid Mech.* **204**, 53 (1987).

³⁶S. E. Guarini, R. D. Moser, K. Shariff, and A. Wray, “Direct numerical simulation of a supersonic turbulent boundary layer at Mach 2.5,” *J. Fluid Mech.* **414**, 1 (2000).

³⁷R. B. Loucks, “An experimental examination of the velocity and vorticity

- fields in a plane mixing layer,” Ph.D. dissertation, University of Maryland, 1998.
- ³⁸A. B. Folz, “An experimental study of the near-surface turbulence in the atmospheric boundary layer,” Ph.D. dissertation, University of Maryland, 1998.
- ³⁹J. A. Mullin and W. J. A. Dahm, “Dual-plane stereo particle image velocimetry measurements of velocity gradient tensor fields in turbulent shear flow I. Accuracy assessments,” *Phys. Fluids* **18**, 035101 (2006); “Dual-plane stereo particle image velocimetry measurements of velocity gradient tensor fields in turbulent shear flow II. Experimental results,” *ibid.* **18**, 035102 (2006).
- ⁴⁰P. S. Bernard and J. M. Wallace, *Turbulent Flow: Analysis, Measurement, and Prediction* (Wiley, Hoboken, NJ, 2002), p. 131.
- ⁴¹R. D. Moser, J. Kim, and N. N. Mansour, “DNS of turbulent channel flow up to $Re=590$,” *Phys. Fluids* **11**, 943 (1999).
- ⁴²B. W. Zeff, D. D. Lanterman, R. McAllister, R. Roy, E. J. Kostelic, and D. P. Lathrop, “Measuring intense rotation and dissipation in turbulent flows,” *Nature (London)* **421**, 146 (2003).
- ⁴³H. M. Blackburn, N. N. Mansour, and B. J. Cantwell, “Topology of fine-scale motions in turbulent channel flow,” *J. Fluid Mech.* **310**, 269 (1996).
- ⁴⁴L. Chevillard, C. Meneveau, L. Biferale, and F. Toschi, “Modeling the pressure Hessian and viscous Laplacian in turbulence: Comparisons with DNS and implications on velocity gradient dynamics,” *Phys. Fluids* **20**, 101504 (2008).
- ⁴⁵J. Jiménez, “Kinematic alignment effects in turbulent flows,” *Phys. Fluids A* **4**, 652 (1992).
- ⁴⁶H. K. Moffatt, “Magnetostatic equilibria and analogous Euler flows of arbitrarily complex topology. Part 1. Fundamentals,” *J. Fluid Mech.* **159**, 359 (1985).
- ⁴⁷M. M. Rogers and P. Moin, “Helicity fluctuations in incompressible turbulent flows,” *Phys. Fluids* **30**, 2662 (1987).
- ⁴⁸J. M. Wallace, J.-L. Balint, and L. Ong, “An experimental study of helicity density in turbulent flows,” *Phys. Fluids A* **4**, 2013 (1992).
- ⁴⁹J. M. Chacin and B. J. Cantwell, “Dynamics of a low Reynolds number turbulent boundary layer,” *J. Fluid Mech.* **404**, 87 (2000).
- ⁵⁰J. Soria, R. Sondergaard, B. J. Cantwell, M. S. Chong, and A. E. Perry, “A study of the fine-scale motions of incompressible time-developing mixing layers,” *Phys. Fluids* **6**, 871 (1994).
- ⁵¹J. M. Wallace, H. Eckelmann, and R. S. Brodkey, “The wall region in bounded turbulent flow,” *J. Fluid Mech.* **54**, 39 (1972).
- ⁵²Y. Andreopoulos and A. Honkan, “An experimental study of the dissipative and vortical motion in turbulent boundary layers,” *J. Fluid Mech.* **439**, 131 (2001).
- ⁵³C. Rosales and C. Meneveau, “A minimal multiscale Lagrangian map approach to synthesize non-Gaussian turbulent vector fields,” *Phys. Fluids* **18**, 075104 (2006).
- ⁵⁴A. Vincent and M. Meneguzzi, “The spatial structure and statistical properties of homogeneous turbulence,” *J. Fluid Mech.* **225**, 1 (1991).
- ⁵⁵E. D. Siggia, “Numerical study of small-scale intermittency in three-dimensional turbulence,” *J. Fluid Mech.* **107**, 375 (1981).
- ⁵⁶Z. S. She, E. Jackson, and S. A. Orzag, “Intermittent vortex structures in homogeneous isotropic turbulence,” *Nature (London)* **344**, 226 (1990).
- ⁵⁷P. Chakraborty, S. Balachandar, and R. J. Adrian, “On the relationships between local vortex identification schemes,” *J. Fluid Mech.* **535**, 189 (2005).
- ⁵⁸J. A. Langford and R. D. Moser, “Optimal LES formulations for isotropic turbulence,” *J. Fluid Mech.* **398**, 321 (1999).
- ⁵⁹J. C. R. Hunt, A. A. Wray, and P. Moin, “Eddies, stream and convergence zones in turbulent flows,” Center for Turbulence Research Annual Report No. CTR-S88, 1988.
- ⁶⁰J. Jeong and F. Hussain, “On the identification of a vortex,” *J. Fluid Mech.* **285**, 69 (1995).
- ⁶¹M. S. Chong, A. E. Perry, and B. J. Cantwell, “A general classification of three-dimensional flow fields,” *Phys. Fluids A* **2**, 765 (1990).
- ⁶²J. Zhou, R. J. Adrian, S. Balachandar, and T. M. Kendall, “Mechanisms for generating coherent packets of hairpin vortices in channel flow,” *J. Fluid Mech.* **387**, 353 (1999).
- ⁶³J. C. Del Alamo, J. Jimenez, P. Zandonade, and R. Moser, “Scaling of the energy spectra of turbulent channels,” *J. Fluid Mech.* **500**, 135 (2004).
- ⁶⁴A. Ferrante, S. Elghobashi, P. Adams, M. Valenciano, and D. Longmire, “Evolution of quasistreamwise vortex tubes and wall streaks in a bubble-laden turbulent boundary layer over a flat plate,” *Phys. Fluids* **16**, S2 (2004); see http://pof.aip.org/pof/gallery/video/2004/901406phf_15MB.mov for an enhanced video.
- ⁶⁵M. M. Rogers and R. D. Moser, “The three-dimensional evolution of a plane mixing layer: the Kelvin-Helmholtz rollup,” *J. Fluid Mech.* **243**, 183 (1992).
- ⁶⁶P. Comte, J. Silvestrini, and P. Begou, “Streamwise vortices in large-eddy simulations of mixing layers,” *Eur. J. Mech. B/Fluids* **17**, 615 (1998).